An Investigation of Raw Data Corrections for Radial Fat-Water Magnetic Resonance Imaging

By

Xuelin Cui

Thesis

Submitted to the Faculty of the

Graduate School of Vanderbilt University

in partial fulfillment of the requirements

for the degree of

MASTER OF SCIENCE

in

Biomedical Engineering

December, 2011

Nashville, Tennessee

Approved:

Edward Brian Welch, Ph.D.

Mark Does, Ph.D.

William Grissom, Ph.D.

ACKNOWLEDGEMENTS

My work could not have been achieved without assistance of a number of people from Vanderbilt University Institute of Imaging Science at Vanderbilt University, Nashville, Tennessee.

Foremost, I would like to record my gratitude to my academic advisor Dr. Edward Brian Welch for his advice, supervision and guidance. His truly scientific attitude has made him precise and passionate in his research and has inspired and enriched my growth as a student. This work would not have been completed without your guidance and support.

I gratefully thank Dr. John C. Gore from Vanderbilt University Institute of Imaging Science for sharing his valuable thoughts with me. I also thank him for always providing me with support and encouragement in various ways. I am deeply indebted to him more than he feels.

Many thanks go to Dr. Mark Dose and Dr. Will Grissom both from Department of Biomedical Engineering at Vanderbilt for offering me insightful comments.

Finally, and most importantly, I would like to thank my wife Yiling Zhang. Her support, encouragement, quiet patience and unwavering love were undeniably the bedrock upon which my life has been. I thank my parents, Houyin Cui and Xiaoyu Huang, for their faith in me and allowing me to be as free as I wanted. It was under their watchful eye that I gained so much drive and an ability to tackle challenges head on.

ABSTRACT

In addition to the inherent chemical phase shift between different proton species, fat-water MRI k-space raw data are corrupted by several sources such as magnetic field inhomogeneity; chemical shift phase accumulated during the data readout window and trajectory shifts due to non-ideal gradient performance. NMR signal can be modeled within a single voxel as the mixture of different type protons with all corrupting factors clearly defined. If multiecho data are acquired, the evolving fat-water signal can be described as a linear system which can be unmixed. A reversed readout-based method is investigated in this work to correct the field inhomogeneity for radial fat-water MRI data. In the Cartesian case, the field map can be estimated using an iterative approach when other corrupting factors are precisely modeled. In addition, accurate fat-water signal modeling includes the use of a multipeak fat spectrum, and precise sampling time information. Multipeak fat spectrum information is obtained from nuclear magnetic spectroscopy, and the precise sampling time information is based on the employed pulse sequence. On the other hand, fat-water image reconstruction from radial trajectory data requires non-uniform Fourier transformation including regridding, density correction and interpolation. All these procedures are inserted as a part of radial fat-water separation. The artifact caused by imperfect gradients for radial MRI is also discussed and corrected in this work. Reconstruction results for both Cartesian and radial data with all corrections applied are displayed and compared.

TABLE OF CONTENTS

Page

LIST OF TABLES

Table Page

LIST OF FIGURES

Figure Page

CHAPTER 1

INTRODUCTION

1.1 MRI Basics

It is widely considered that magnetic resonance imaging (MRI) is one of the most innovative imaging techniques available in the 21st century. MRI serves as a major medical imaging system alongside other modern imaging modalities such as CT, ultrasound and PET and SPECT. MRI is based on the physics phenomenon that an external magnetic field and an excitation radio frequency (RF) pulse can trigger the object to emit signal. Major components of a MRI system include an external static magnetic field in which the object is placed; a RF transmit coil that excites net magnetization into the transverse plane; magnetic gradients encoding spatial information along different directions; and RF coils that receive MRI signal.

When an external static magnetic field is applied, protons in the object start precessing about the direction of the magnetic field with a constant frequency. This frequency is called the Larmor frequency, which is determined both by the strength of external magnetic field and by the gyromagnetic ratio. The gyromagnetic ratio is strictly related to nuclei species, which leads to the fact that protons in different nuclei species, such as H^1, C^{13}, N^{15} or P^{31}, precess at different rate even when experiencing the same magnetic field strength. The precessing protons will then be deviated by a RF pulse from its equilibrium state. The net magnetization will be nutated by the RF pulse into the transverse plane perpendicular to the direction of the

external static magnetic field, which is similar to resonance. After the net magnetization is lying in the transverse plane, another magnetic field, the magnetic field gradient, is applied to differentiate spatial information at one location from the other. The typical spatial gradients include slice selective, phase, and frequency encoding (readout) to cover spatial information of the object on a 2D plane. A 3D acquisition utilizes a slab selective gradient and a second phase encoding gradient.

MRI systems often do not work as perfectly in reality as they are described in theories. Artifacts, usually caused by various reasons such as magnetic and RF field inhomogeneity, non-ideal gradient performance, or other physics/physiological limitations, are commonly found in MRI images. An artifact can be defined as any feature in an image which misrepresents the object in the field of view (FOV). This could be a erroneous bright signal outside the object, or lack of signal where there should be something. It could also be a reconstructed image with streaks that do not exist in the real object or with misplaced object signal appearing at a different location in the reconstructed than it actually is. A large group of MR artifacts appear as ‘ghost’ images, where a faint copy of the object appears in the image displaced in one direction or another. In general artifacts are critical in MR image reconstruction.

1.2 Chemical Shift Imaging

In nuclear magnetic resonance (NMR), the chemical shift describes the dependence of nuclear magnetic energy levels on the electronic environment in a molecule [1] [2]. Microscopically, electrons will start precess when an external magnetic field is induced. The precessing particles, according to Lenz’s law, will then generate a new magnetic field opposing to the induced one. The new magnetic field has a smaller strength than the original

one such that the net magnetic field strength is weakened by a fraction σ. This faction, also called shielding constant σ, is specific to molecular structures. Quantitatively, this shielding constant can be estimated if shift in PPM between two species along resonance frequency axis is known. This phenomenon that frequency is altered by the electron environments is recognized as paramagnetic shielding in physics.

Since the magnetic field strength is changed by the electron environments, the nuclear magnetic resonance (NMR) frequency will be different as well. This difference will depend on the strength of the static magnetic field B_0, used to perform the NMR spectroscopy. The greater the value of B_0, the greater the frequency difference will be. This relationship could make it difficult to compare NMR spectra taken on spectrometers operating at different field strengths, so the term chemical shift is reported in part per million (PPM) [3].

The chemical shift of a nucleus is defined relative to the standard as the difference between the resonance frequency of the nucleus and a standard [3].

$$\delta = \frac{\left(f - f_{ref}\right)\times 10^6}{f_{ref}}, \qquad 1.1$$

where f is the frequency of the observed species, and f_{ref} is the reference frequency. In NMR spectroscopy, this standard is often tetramethylsilane, abbreviated TMS. In the body, since there is no TMS, water protons are usually considered the reference [3].

It should also be noted that artifact in MRI caused by chemical shift occurs either in slice selective direction, or along readout direction in which frequency information is encoded. Although chemical shift happens in phase encoding direction as well, it does not accumulate. This is due to the fact that MRI signal is repeatedly excited to acquire separate phase

encodes. Since it is a new excitation and new echo, chemical shift in the phase encoding direction does not change from one signal to the next. This implies that chemical shift artifact has no impact on signal in the phase encoding direction.

Because spatial information is coded based on resonance frequency in the frequency encoding direction, misregistration arises when chemical shift exist. This means multiple chemical species can cause image signal to displace from its original location in spatial domain, which can be mathematically explained by the Fourier transform shift theorem. Chemical shift is notorious in MRI as one of the main artifacts alongside others such as motion, RF inhomogeneity and B_0 inhomogeneity. Figure 1.1 [4] is an example showing the artifact caused by fat water chemical shift [4]:

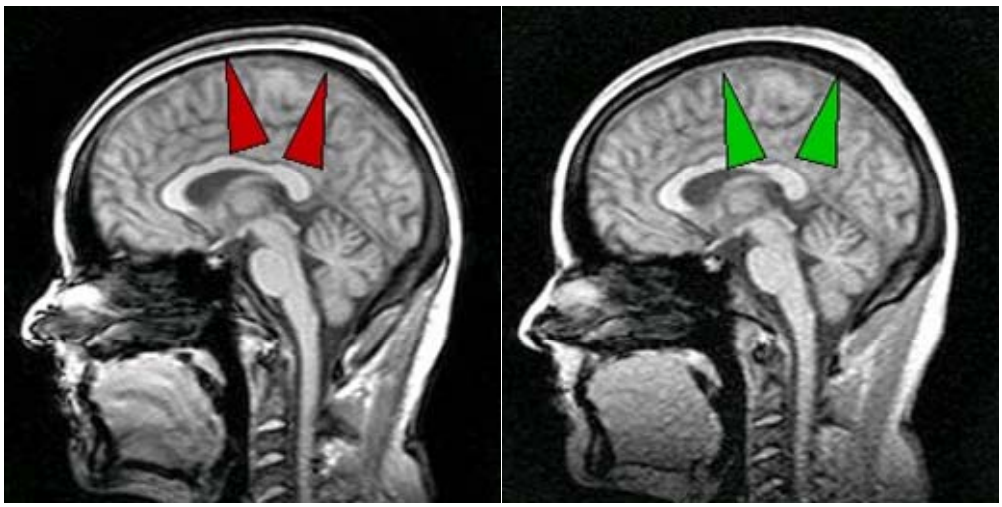

Figure 1.1. An example of artifact caused by chemical shift (cited from [4]).

In Figure 1.1, the left panel shows that the chemical shift artifact is visible as a small dark or bright border at the interfaces of bone, fat and muscle indicated by red arrows. This scan was acquired with maximum water fat shift. Right panel shows the same slice as left panel, but

scanned with minimum water fat shift. As is indicated by green arrows, the interface borders are smaller, but the higher sampling rate that minimizes water fat shift lowers the signal to noise ratio [4] [5].

In the human body, there mainly are two organic molecule types containing hydrogen: fat and water. Fat-water imaging has been demonstrated in many clinical applications such as quantification of fat in tissues. Although numerous works have been accomplished in fat water separation, it is still considered noticeably more challenging than many image processing topics in MRI. Fat water separation can be more complicated when other factors, such as difference in sampling time and field inhomogeneity, are introduced. In addition, fat water separation from non-Cartesian k-space data increases the difficulty of the reconstruction. Especially static field inhomogeneity estimation is a rather challenging topic.

To understand the cause of artifacts in fat water imaging, an investigation about the chemical structure of fat and water is in order. Fat comprises hydrogen atoms linked to carbon such as methylene protons in triglycerides $([-CH_2-]_n)$, which make up large molecules. The large molecules in fat have a slow rate of molecular motion due to inertia of the large molecules. They also have a low inherent energy which means they are able to absorb energy efficiently. Water comprises hydrogen atoms linked to oxygen $[-OH]$. Water consists of small molecules with little inertia that have a high rate of molecular motion. Water molecules have a high inherent energy which means they are not able to absorb energy efficiently [4]. On the other hand, the electron density around each proton is different in fat and water molecules. Triglyceride structure provides more diamagnetic shielding for methylene protons than for protons in water. This paramagnetic shielding results in a lower precession rate for protons in fat.

Chemical shift between fat and water causes misregistration along the readout direction. Particularly, water protons at location x_w with gradient strength G_x precess at frequency f_w:

$$f_w = \frac{\gamma}{2\pi} G_x x_w, \quad 1.2$$

Where, γ is the value of gyromagnetic ratio. Due to chemical shift effect, fat protons precess at a lower frequency f_w:

$$f_f = \frac{\gamma}{2\pi} G_x x_w - \delta \frac{\gamma}{2\pi} B_0, \quad 1.3$$

Where, δ is the chemical shift measured in ppm, and B_0 is the strength of the external static magnetic field. Therefore, a displacement will be observed in reconstructed image where fat signal moves away from its true location. If water is considered the reference frequency, the displacement is:

$$\Delta x = x_w - x_f = \delta \frac{B_0}{G_x}, \quad 1.4$$

The displacement is proportional to the strength of operating frequency. Since fat has 3.5 ppm chemical shift downfield from water, it corresponds to approximately 220 Hz at 1.5T and 440 Hz at 3.0T. For example, in a 3.0T static external magnetic field, if the bandwidth is 1340 Hz/pixel, and if the pixel size is 1 mm by 1 mm, the chemical shift will cause 0.33mm displacement between fat image and water image.

1.3 Radial MRI and Its Reconstruction

Radial MRI is one of the most common non-Cartesian trajectories in MRI system today. It is typically composed of a group of equally spaced radial samplings that overlap at the center of k-space, as depicted in Figure 1.2. Radial MRI has gained popularity due to several advantages: First of all, each spoke of a radial data set contains an equal amount of low and high frequencies, which leads to advantageous undersampling properties. Second, the Fourier transform of each spoke corresponds to a projection through the object in an angle perpendicular to the direction of the projection. This relationship is a direct consequence of the Fourier Projection-Slice Theorem and assigns a geometric meaning to each single k-space diagonal. It allows for the adoption of reconstruction techniques from transmission tomography including consistency criteria, which can be used for artifact correction. Third, radial trajectories oversample the central portion of k-space which, though apparently inefficient, turns out to be beneficial in certain practical scenarios. Moreover, the central oversampling may be exploited for multicontrast MRI and parallel imaging by reconstructing multiple low-resolution images from undersampled data sets [6] [7].

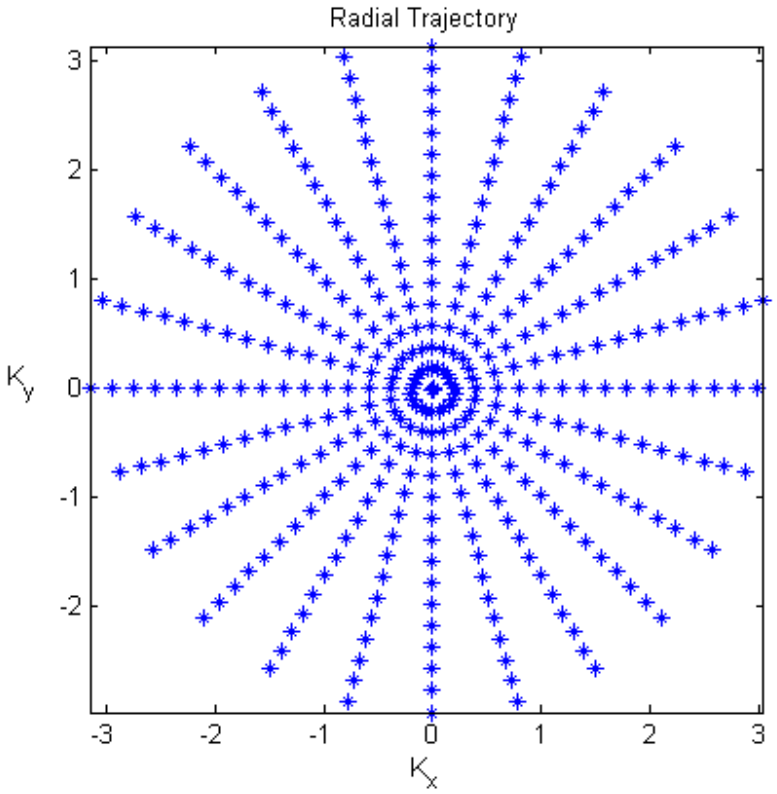

Figure 1.2. Trajectory of Radial MRI in k-space.

MRI data on scanners is recorded in k-space, which is the Fourier transform of the image data. A 2D image can be considered a 2D digitized function $f(x, y)$ from a signal processing perspective. There are two primary signal domains in MRI: the spatial domain and the spatial frequency domain (k-space), which are conjugates of each other via Fourier transform.

Radial MRI also has image space and k-space. Its image space is represented in Cartesian grid, whereas its k-space data are arranged in sinogram format. The sinogram format comprises parallel projections across all projection angles lined up next to each other. Each parallel projection is defined as the line integral along across the object at a projection angle θ. The ensemble of all projections is known as a sinogram. One of the fundamental

principals in radial MRI reconstruction is the Fourier Projection-Slice Theorem, which states that the Fourier transform of a parallel projection of an object $f(x, y)$ obtained at angle θ equals a line in a 2D Fourier transform of $f(x, y)$ taken at the same angle [8]. The Fourier Projection-Slice Theorem is illustrated in Figure 1.3 [8]:

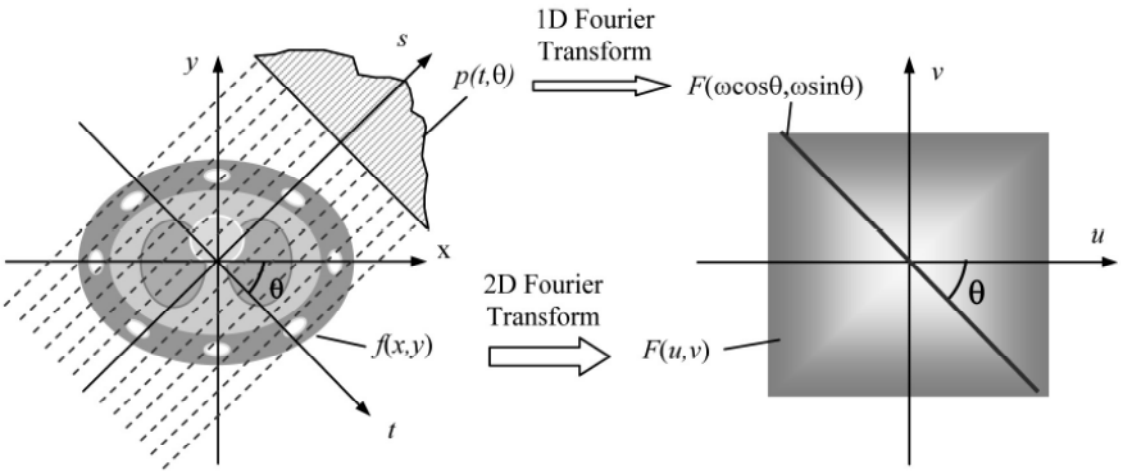

Figure 1.3. Illustration of the Fourier Projection-Slice Theorem.

where θ is the projection angle, t is the position along projections, ω is the digital frequency, and $F(k_x, k_y)$ is MR signal in k-space. The Fourier Projection-Slice Theorem can be formulated in Equation 1.5 [8]:

$$P(\omega,\theta)=\int_{-\infty}^{\infty}\int_{-\infty}^{\infty} f(x,y)e^{-j2\pi\omega(x\cos\theta+y\sin\theta)}dxdy = F(\omega\cos\theta,\omega\sin\theta), \qquad 1.5$$

where, $k_x=\omega\cos\theta, k_y=\omega\sin\theta$ and $F(\omega\cos\theta,\omega\sin\theta)$ is the 2D Fourier transform of $f(x,y)$. Therefore, the reconstructed image, or the inverse 2D Fourier transform of k-space data, can be represented in Equation 1.6 [8]:

$$f(x,y)=\int_{-\infty}^{\infty}\int_{-\infty}^{\infty}F(k_x,k_y)e^{j2\pi(xk+yk_y)}dk_x dk_y, \quad 1.6$$

where $f(x,y)$ is the digital MRI image, and $F(k_x,k_y)$ is the MR signal collected in k-space with coordinates k_x and k_y. By replacing $k_x=\omega\cos\theta$ and $k_y=\omega\sin\theta$ in Equation 1.5, Equation 1.5 evolves to Equation 1.7 [8]:

$$f(x,y)=\int_{-\infty}^{\infty}\int_{-\infty}^{\infty}F(\omega\cos\theta,\omega\sin\theta)e^{j2\pi(x\omega\cos\theta+y\omega\sin\theta)}d\theta d\omega, \quad 1.7$$

Inserting the conclusion in Equation 1.4 into Equation 1.6 to obtain Equation 1.8 [8]:

$$f(x,y)=\int_{0}^{2\pi}d\theta\int_{-\infty}^{\infty}P(\omega,\theta)e^{j2\pi(x\omega\cos\theta+y\omega\sin\theta)}\omega d\omega, \quad 1.8$$

Equation 1.7 can be further simplified as following noticing that $P(\omega,\theta+\pi)=P(-\omega,\theta)$ to obtain Equation 1.9 [8]:

$$f(x,y)=\int_{0}^{\pi}d\theta\int_{-\infty}^{\infty}P(\omega,\theta)|\omega|e^{j2\pi\omega}\omega d\omega, \quad 1.9$$

Here, $P(\omega,\theta)$ is the Fourier transform of the projection at angle. The inside integral is the inverse Fourier transform of the quantity $P(\omega,\theta)|\omega|$. In the spatial domain, it represents a projection filtered by a function whose frequency domain response is $|\omega|$, and is therefore called a “filtered projection” [6]. $|\omega|$ is often referred to as “Ram-Lak” filter [8].

1.4 Fat Water Separation

1.4.1 Two-Point and Three-Point Dixon Methods

The fact that MR signal from human tissue is primarily contributed by protons in water and lipids allows us to model the signal from a single voxel as in Equation 1.10 [9]:

$$s_n = w + fe^{j\omega_f TE_n}, \tag{1.10}$$

where, s_n is the signal at nth echo, w is complex water signal component, f is the complex fat signal component, ω_f is the off-resonance frequency caused by chemical shift and TE_n is the nth echo time. Since only two species are under consideration in this model, water is regarded as on resonance, whereas fat is off resonance.

The simplest way to estimate water and lipids signal is to acquire two images at nth echo time TE_n where $\omega_f TE_n = 0, \pi$ mod 2π . Here mod represents modulo operation. This process results in a "0 image" and a "π image" [10]:

$$s_1 = w + f, \tag{1.11}$$

$$s_2 = w - f, \tag{1.12}$$

Water and fat signal can then be estimated as in Equation 1.13 and Equation 1.14 [9]:

$$\hat{w} = \frac{1}{2}(s_1 + s_2). \tag{1.13}$$

$$\hat{f} = \frac{1}{2}(s_1 - s_2), \tag{1.14}$$

Above is the Two-Point Dixon method, which separates water and fat signal using a combination of images from a two-echo acquisition. However, aside from chemical shift effect, there are other components that compromise the separation of the water and fat image. For example, the underlying static magnetic field inhomogeneity, the T_2^* decay of signal and the inhomogeneous penetration of the imaging volume by radiofrequency pulses [7]. Among these factors, the problem of the static magnetic field inhomogeneity is by far the most important. Other factors, such as the estimation and correction for T_2^* degrading the separation between fat and water, is of secondary concern [9]. In Two-Point Dixon model, the signal can be extended if field inhomogeneity is added:

$$s_1 = (w + f)e^{j\psi TE_1} \tag{1.15}$$

$$s_2 = (w - f)e^{j\psi TE_2} \tag{1.16}$$

where ψ is the magnetic field inhomogeneity frequency measured in radians per second. The estimate of water image in Equation 1.13 then becomes [8]:

$$\hat{w} = \frac{1}{2}\left[s_1\left(1 + e^{j\psi(TE_2 - TE_1)}\right) + s_2\left(1 - e^{j\psi(TE_2 - TE_1)}\right)\right]. \tag{1.17}$$

It can be seen that even for a small off-resonance small angle, the water estimate will be significantly contaminated by the fat component in the voxel.

One solution to manage this primary concern caused by magnetic field inhomogeneity is to

add an additional measurement to allow the magnetic field inhomogeneity quantity ψ to be estimated [11]. If one more echo image is acquired, the Two-Point Dixon method will become the Three-Point Dixon method which is mathematically formulated in Equation 1.18 through Equation 1.20:

$$s_1 = (w + f)e^{j\psi TE_1} \quad 1.18$$

$$s_2 = (w - f)e^{j\psi TE_2} \quad 1.19$$

$$s_3 = (w + f)e^{j\psi TE_3} \quad 1.20$$

If the echo time is symmetrically distributed, $\psi TE_3 = 3\psi TE_1$ and $\psi TE_2 = 2\psi TE_1$, and the increment of phase between two consecutive echoes is identical. Thus, the phase increment ϕ between echoes can be estimated by from s_1 and s_3:

$$2\hat{\phi} = \arg(s_1^* s_3), \quad 1.21$$

where, $\hat{\phi}$ is the estimate of ϕ, $\arg(\cdot)$ denotes the angle between two vectors, and s_1^* is the complex conjugate of s_1.

s_2 can then be phase corrected based on the estimate of the phase accrual due to field inhomogeneity, and combined with s_1 to obtain the estimate of water and fat signal [9]:

$$\hat{w} = \frac{1}{2}\left[s_1 + s_2 e^{-j\hat{\phi}}\right] \quad 1.22$$

$$\hat{f} = \frac{1}{2}\left[s_1 - s_2 e^{-j\bar{\phi}}\right]. \qquad 1.23$$

However, a closer investigation of the above conclusion raises another problem. By replacing s_1 and s_2 with the summation of water and fat signals in Equation 1.22 and Equation 1.23, one will have following representations [9]:

$$\hat{w} = \frac{1}{2}\left[w\left(1 + e^{j(\phi-\bar{\phi})}\right) + f\left(1 - e^{j(\phi-\bar{\phi})}\right)\right] \qquad 1.24$$

$$\hat{f} = \frac{1}{2}\left[w\left(1 - e^{j(\phi-\bar{\phi})}\right) + f\left(1 + e^{j(\phi-\bar{\phi})}\right)\right] \qquad 1.25$$

These equations indicates that the estimate of water and fat signal is correct only when $\hat{\phi} = \phi$.

The Dixon method provides an idea how the fat-water signal in a single voxel is modeled. It also explains how distortion occurs in spatial domain or k-space due to phase accrual. Further analysis on fat-water separation in Chapter 2 is also an extension from Dixon method.

CHAPTER 2

METHODS, MATERIALS AND RESULTS

The novel contribution in this work is that the field inhomogeneity correction for radial MRI raw data was investigated. A reversed readout gradient method based method studied in [12] was applied to process radial MRI raw data. The numerical integration technique in this work was modified to Runge-Kutta-Felhberg 5th order method.

Two fat-water phantoms, the Marcol 86 Exxon mineral oil phantom and the peanut oil phantom, were used in experiments to test separation algorithms. During the experiments, the peanut oil phantom behaves more sensitive to the field inhomogeneity than the mineral oil phantom. The comparison of the separation results between the two phantoms demonstrated the importance of correction both in k-space domain and image domain.

2.1 Iterative Least-Squares Estimation Method

As introduced in the previous chapter, the fat water separation is a voxel-wise operation based on knowledge of the field inhomogeneity and chemical shift. Field inhomogeneity is one of the major MRI artifacts that noticeably impacts the quality, such as tissue interface or object geometry, of the final reconstruction. It is caused by B_0 inhomogeneity, paramagnetic or ferromagnetic implants [13] [14]. In 2004, Scott Reeder proposed an iterative algorithm to separate fat and water in a single voxel. This algorithm is called iterative lease-squares

estimation method, or simply the IDEAL algorithm. It processes Cartesian k-space data to generate estimates of the field inhomogeneity map and fat and water images iteratively. The data acquired originally in Reeder's work was fast spin echo data with echo duration less than 1ms. The short echo time has advantages including high signal to noise ratio (SNR), less T_2^* effect and favorable contrast behavior [15].

In the IDEAL method, the signal in a individual voxel is modeled as the summation of the fat signal and water signal with the summation biased by the field inhomogeneity as Equation 2.1 [15]:

$$s(t) = \left(\sum_{j=1}^{M} \rho_j e^{i2\pi\Delta f_j t} \right) e^{i2\pi\psi t}, \qquad 2.1$$

where $s(t)$ is the signal intensity in a single voxel at time t, M is the number of the chemical species, ρ_j is the image for j th species, Δf_j is the chemical shift compared to water and ψ is the field inhomogeneity. At the n th echo time t_n, Equation 2.1 becomes [15]:

$$s(n) = \left(\sum_{j=1}^{M} \rho_j e^{i2\pi\Delta f_j t_n} \right) e^{i2\pi\psi t_n}, \qquad 2.2$$

The reconstruction of fat and water image cannot be conducted until the field inhomogeneity is corrected. By assuming field inhomogeneity as ψ, the estimated combination of water and fat signal can be formulated in Equation 2.3 [15]:

$$\widehat{s}_n = s_n e^{i2\pi(-\psi)t_n} = \sum_{j=1}^{M} \rho_j e^{i2\pi\Delta f_j t_n}, \qquad 2.3$$

For $n = 1, \cdots, N$; Equation 2.3 can be formatted using matrix representation listed below [15]:

$$\begin{bmatrix} \hat{s}_1^R \\ \hat{s}_2^R \\ \vdots \\ \hat{s}_4^R \\ \hat{s}_1^I \\ \hat{s}_2^I \\ \vdots \\ \hat{s}_4^I \end{bmatrix} = \begin{bmatrix} c_{11} & -d_{11} & c_{21} & -d_{21} & \cdots & c_{M1} & -d_{M1} \\ c_{12} & -d_{12} & c_{22} & -d_{22} & \cdots & c_{M2} & -d_{M2} \\ \cdots & \cdots & \cdots & \cdots & \cdots & \cdots & \cdots \\ c_{1N} & -d_{1N} & c_{2N} & -d_{2N} & \cdots & c_{MN} & -d_{MN} \\ d_{11} & c_{11} & d_{21} & c_{21} & \cdots & d_{M1} & c_{M1} \\ d_{12} & c_{12} & d_{22} & c_{22} & \cdots & d_{M2} & c_{M2} \\ \cdots & \cdots & \cdots & \cdots & \cdots & \cdots & \cdots \\ d_{1N} & c_{1N} & d_{2N} & c_{2N} & \cdots & d_{MN} & c_{MN} \end{bmatrix} \begin{bmatrix} \rho_1^R \\ \rho_1^R I \\ \rho_2^R \\ \rho_2^I \\ \vdots \\ \rho_3^R \\ \rho_3^I \end{bmatrix}, \quad 2.4$$

where ρ_j^R is the real part of the jth species, ρ_j^I is the imaginary part of the jth species, $c_{jn} = cos(2\pi\Delta f_j t_n)$ and $d_{jn} = sin(2\pi\Delta f_j t_n)$.

Equation 2.4 can be simply written as:

$$\hat{S} = A\rho, \quad 2.5$$

Thus each species, for example water and fat, can be calculated as following:

$$\rho = \left(A^T A\right)^{-1} A^T \hat{S} \quad 2.6$$

On the other hand, Equation 2.3 can further be analyzed using Taylor expansion to produce the following [15]:

$$\hat{\tilde{s}}_n^R = \hat{s}_n^R - \sum_{j=1}^{M}\left(\hat{\rho}_j^R c_{jn} - \hat{\rho}_j^I d_{jn}\right) = 2\pi\Delta\psi t_n \sum_{j=1}^{M}\left(-\hat{\rho}_j^R d_{jn} - \hat{\rho}_j^I c_{jn}\right) + \sum_{j=1}^{M}\left(\hat{\rho}_j^R c_{jn} - \hat{\rho}_j^I d_{jn}\right) \quad 2.7$$

and

$$\hat{\tilde{s}}_n^I = \hat{s}_n^I - \sum_{j=1}^{M}\left(\hat{\rho}_j^R d_{jn} + \hat{\rho}_j^I c_{jn}\right) = 2\pi\Delta\psi t_n \sum_{j=1}^{M}\left(\hat{\rho}_j^R c_{jn} - \hat{\rho}_j^I d_{jn}\right) + \sum_{j=1}^{M}\left(\hat{\rho}_j^R d_{jn} + \hat{\rho}_j^I c_{jn}\right). \quad 2.8$$

Equation 2.7 and 2.8 can be combined together as matrix multiplication:

$$\begin{bmatrix} \hat{s}_1^R \\ \hat{s}_2^R \\ \vdots \\ \hat{s}_4^R \\ \hat{s}_1^I \\ \hat{s}_2^I \\ \vdots \\ \hat{s}_4^I \end{bmatrix} = \begin{bmatrix} g_{11}^R\ c_{11} & -d_{11} & c_{21} & -d_{21} & \cdots & c_{M1} & -d_{M1} \\ g_{12}^R\ c_{12} & -d_{12} & c_{22} & -d_{22} & \cdots & c_{M2} & -d_{M2} \\ \cdots\ \cdots & \cdots & \cdots & \cdots & \cdots & \cdots & \cdots \\ g_{1N}^R\ c_{1N} & -d_{1N} & c_{2N} & -d_{2N} & \cdots & c_{MN} & -d_{MN} \\ g_{11}^I\ d_{11} & c_{11} & d_{21} & c_{21} & \cdots & d_{M1} & c_{M1} \\ g_{12}^I\ d_{12} & c_{12} & d_{22} & c_{22} & \cdots & d_{M2} & c_{M2} \\ \cdots\ \cdots & \cdots & \cdots & \cdots & \cdots & \cdots & \cdots \\ g_{1N}^I\ d_{1N} & c_{1N} & d_{2N} & c_{2N} & \cdots & d_{MN} & c_{MN} \end{bmatrix} \begin{bmatrix} \Delta\psi \\ \Delta\rho_1^R \\ \Delta\rho_1^R \\ \Delta\rho_2^R \\ \Delta\rho_2^I \\ \vdots \\ \Delta\rho_3^R \\ \Delta\rho_3^I \end{bmatrix}, \quad 2.9$$

Equation 2.9 in simple matrix notation is:

$$\hat{\tilde{S}} = BY. \quad 2.10$$

The critical point in IDEAL algorithm is the update of the field inhomogeneity map: $\Delta\psi$, which is saved in another matrix Y . From Equation 2.9, Y can be solved in Equation 2.11 [15]:

$$Y = \left(B^T B\right)^{-1} B^T \hat{\tilde{S}}. \quad 2.11$$

The IDEAL method starts from a initial guess for field inhomogeneity map, ψ_0 , then it iteratively solves for the estimation of the field inhomogeneity map. For a single receive channele acquisition, the steps of determining field map are described in [15] as following:

1. Estimate the signal from each chemical species using Equation 2.6 and an initial guess for the field map, ψ_0 . A useful initial guess for ψ_0 is zero (Hz).

2. Calculate the error to the field map, $\Delta\psi$, using Equation 2.11.

3. Update $\psi = \psi_0 + \Delta\psi$.

4. Recalculate $\hat{S}$ using Equation 2.5 with the new estimate of ψ .

5. Repeat the preceding three steps until $\Delta\psi$ is smaller than tolerance, for example 1Hz.

6. Spatially filter (smooth) the final field map, ψ , with a low-pass filter.

7. Recalculate the final estimate of each chemical species image with Equation 2.6.

8. Filter the field map to reduce noise performance.

The previous steps are the original work from Reeder in [15]. It explains the basic procedures of how the field map is estimated from single-coil Cartesian data.

Although the estimate of different species was also described in the original IDEAL method, the fat water separation can be improved if the signal is better modeled. This will be introduced in next section.

2.2 Radial Fat Water Imaging Separation

In order to accurately separate fat and water signal in a single voxel, many factors, such as field inhomogeneity, echo time, and chemical shift, need to be known. The original IDEAL method concentrated on image domain distortion, but some k-space based distortion was not processed. This IDEAL based, but improved, method was introduced by Ethan Brodsky in 2008 [16], which allows signal separation using the actual acquisition time of each k-space

point, rather than lumping all k-space acquisition times together into the single time of echo. Compared to [15], [16]primarily corrects distortion occurring in k-space due to chemical shift, which manifest as larger errors in non-Cartesian readouts.

Similar to the signal model in [15], the MR signal in a single voxel is described in Equation 2.12 [16]:

$$s(r,t_n)=\left(\sum_{m=1}^{M}\rho_m(r)e^{i2\pi\Delta f_m t_n}\right)e^{i2\pi\psi(r)t_n}, \qquad 2.12$$

where, $s(r,t_n)$ is the signal at r th location, $\rho_m(r)$ is the signal from m th at r th location, species Field map, Δf_m is the chemical shift in ppm for m th species, t_n is echo time and $\psi(r)$ is the field map. Prior to any further processing, the field map needs to be removed from the signal [16]:

$$\hat{s}(r)=s(r)e^{i2\pi[-\psi(r)]t_n}=\left(\sum_{m=1}^{M}\rho_m(r)e^{i2\pi\Delta f_m t_n}\right), \qquad 2.13$$

The demodulated signal is inversely Fourier transformed back into k-space. In k-space, echo time information is carefully used to refine the signal model as compared to that in original IDEAL method. Particularly, instead of using a “bulk echo time” t_n, a new term, $\tau_{k,n}$ is introduced. The $\tau_{k,n}$ is associated with each k-space location and with each echo time. It indicates the relative time delay from a single k-space sampling location where the signal is being acquired to the center of the current echo time. With this new factor added, the Fourier transformed signal becomes [16]:

$$\hat{s}(\tau_{k,n},k)=\sum_{m=1}^{M}\rho_m(k)e^{i2\pi\Delta f_m(t_n+\tau_{k,n})}, \tag{2.14}$$

This new term, $\tau_{k,n}$, describes the acquisition time for each sample point. Rewriting Equation 2.14 as matrix representation gives following Equation 15 [16]:

$$\begin{bmatrix}\hat{s}_1(k)\\ \hat{s}_2(k)\\ \vdots\\ \hat{s}_4(k)\end{bmatrix}=\begin{bmatrix}c_{11}d_{11}(k) & c_{21}d_{21}(k) & \cdots & c_{M1}d_{M1}(k)\\ c_{12}d_{12}(k) & c_{22}d_{22}(k) & \cdots & c_{M2}d_{M2}(k)\\ \vdots & \vdots & \ddots & \cdots\\ c_{1N}d_{1N}(k) & c_{2N}d_{2N}(k) & \cdots & c_{MN}d_{MN}(k)\end{bmatrix}\begin{bmatrix}\rho_1(k)\\ \rho_2(k)\\ \vdots\\ \rho_2(k)\end{bmatrix}, \tag{2.15}$$

where $c_{mn}=e^{i2\pi\Delta f_m t_n}$ and $d_{mn}(k)=e^{i2\pi\Delta f_m\tau_{k,n}}$. Equation 2.15 can also simply be represented as [16]:

$$\hat{S}(k)=A_k\rho(k), \tag{2.16}$$

So the signal of each species can be solved by [16]:

$$\hat{\rho}(k)=A_k^{+}\hat{S}(k), \tag{2. 17}$$

where, A_k^{+} represents the Moore-Penrose pseudo inverse of A_k, and [16]

$$A_k^{+}=\left(A_k^H A_k\right)^{-1}A_k^H, \tag{2.18}$$

where, A_k^H is the Hermitian transpose of A_k.

The final separation results, $\hat{\rho}_m(r)$, can be obtained by performing an inverse Fourier

transform on the k-space estimate $\hat{\rho}_m(k)$. $\hat{\rho}_m(r)$ is free of chemical shift effects [16].

2.3 Multipeak Signal Model

It is commonly seen that more that a fatty tissues, or even fat-water phantom, contains more than one type of lipid proton. For example, chemical shift documented between fat and water is usually 3.5 ppm, but this is actually an approximation using the primary peak. When analyzed with nuclear magnetic resonance spectroscopy, multiple lipid proton peaks are detected around 3.5ppm (about 440Hz at 3.0T). Thus the true chemical shift of fatty substance will be altered from its primary peak. This fact suggests that prior knowledge from nuclear magnetic resonance spectroscopy is helpful for better fat water imaging results.

From previous discussion, it is can be seen that the chemical shift information for one species only appears once as Δf_j in signal model. If there are multiple peaks; they must be combined together in some way to achieve more accurate separation.

A multipeak model was presented in [16], where the spectrum of each species is first normalized such that the area under the spectrum curve is unity [16]:

$$\int_{-\infty}^{\infty} a_m(f)df = 1, \tag{2.19}$$

where $a_m(f)$ is the spectrum for the m th species as a function of frequency. Equation 2.19 can be plugged into Equation 2.14 to replace the chemical shift frequency with a better representation to get the Equation 2.20 [16]:

$$\hat{s}(\tau_{k,n},k)=\sum_{m=1}^{M}\rho_m(k)\int_{-\infty}^{\infty}a_m(f)e^{i2\pi\Delta f_m(t_n+\tau_{k,n})}df, \quad 2.20$$

In reality, the multipeak resonance frequency is modeled as a weighted summation of delta functions with each centered on one single peak. Suppose the total number of the peaks is P_m, and the weighting factor of pth peak in mth species is $r_{m,p}$, then all weighting factors sum to unity [16]:

$$\sum_{p=1}^{P_m}r_{m,p}=1, \quad 2.21$$

The signal in Equation 2.20 can be rewritten as [16]:

$$\hat{s}(\tau_{k,n}k)=\sum_{m=1}^{M}\rho_m(k)\sum_{p=1}^{P_m}r_{m,p}e^{i2\pi\Delta f_m(t_n+\tau_{k,n})}, \quad 2.22$$

Equation 2.20 can also be viewed as the summation of Fourier transform of all species. The phase factors c and d defined where in continuous are also changed as [16]:

$$c_{mn}=\int_{-\infty}^{\infty}a_m(f)e^{i2\pi ft_n}df, \quad 2.23$$

$$d_{mn}(k)=\int_{-\infty}^{\infty}a_m(f)e^{i2\pi f\tau_{k,n}}df, \quad 2.24$$

In the discrete case, Equation 2.23 and 2.24 [16] become Equation 2.25 and 2.26 [16], respectively :

$$c_{mn} = \sum_{p=1}^{P_m} r_{m,p} e^{i2\pi\Delta f_{m,p} t_n}, \quad 2.25$$

$$d_{mn}(k) = \sum_{p=1}^{P_m} r_{m,p} e^{i2\pi\Delta f_{m,p} \tau_{k,n}}, \quad 2.26$$

In both cases, the complex coefficient matrix A_k is then calculated as in Equation 2.15, and $\hat{\rho}_m(k)$ can be unmixed using Equation 2.17. Inverse Fourier transformation finally separates spatial images of each species [16].

2.4 Results of Cartesian Fat-Water Separation

Single channel MRI data, both Cartesian and radial, of a set of phantoms were obtained from a 3T Achieva MRI scanner (Philips Healthcare, Best, The Netherlands). One mineral oil phantom and one peanut oil phantom were acquired with a one channel TR head coil in Cartesian k-space. One mineral oil phantom and one peanut oil phantom were acquired in radial k-space. One regular water phantom was acquired for alternating frequency encoding correction for radial scan.

The mineral oil phantom consists of nearly half water and half mineral oil with mineral oil having less density than water. The peanut oil phantom is made up by mixing water and peanut oil approximately half and half. Peanut oil is also less dense than water.

2.4.1 Data Collection

Cartesian k-space data were acquired with a conventional multiple fast field echo (mFFE) sequence on a 3T Achieva MR scanner (Philips Healthcare, Best, The Netherlands). Field of

view (FOV) was 256 mm×256 mm with 128 phase encode lines and 2 times oversampling along the readout direction. Bandwidth (BW) was 1.3403 kHz/pixel, which made readout duration 0.7461 ms (millisecond). Images were acquired with time of repetition (TR) 71 ms and at 3 echoes with echo times centered at 1.3402 ms, 2.9902 ms and 4.6402 ms, respectively. Two dynamics of data were scanned with each dynamic of data consisting of 12 slices to more easily calculate SNR.

As explained previously, chemical shift of fat water phantoms was represented using a multipeak model which required nuclear magnetic resonance spectroscopy analysis. For the white mineral oil (Marcol 86 Exxon), two peaks, located at 420 Hz and 47 1Hz, were observed at 3 T. The weighting factors for the two peaks were 0.7482 and 0.2518. For the peanut oil phantom, only one distinguished peak is observed at 432 Hz. It should be mentioned that multipeak models are neglected for the peanut oil phantom since the amplitude of other peaks are too small compared to the major peak. Figure 2.1 illustrates the multipeak model for mineral oil with water “on resonance”:

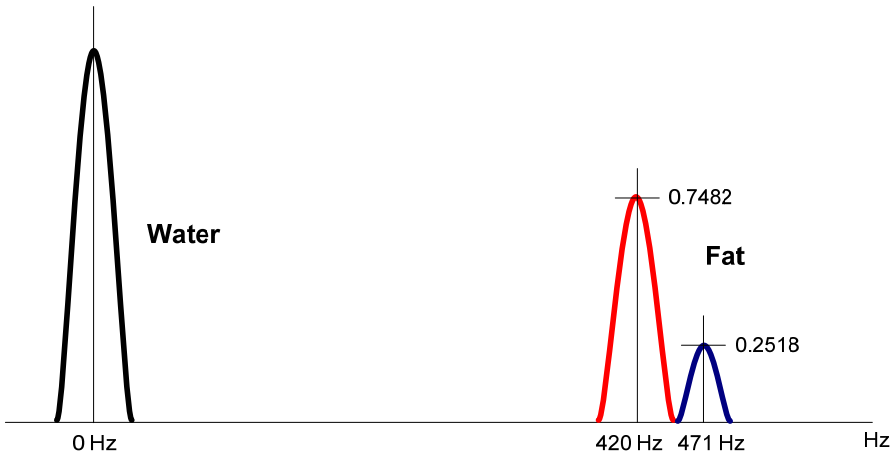

Figure 2.1. Multipeak model at 3 T for the mineral oil phantom. Water is “on resonance”; Fat has two peaks located at 420 Hz and 471 Hz with amplitude weighting 0.7482 and 0.2581.

2.4.2 Separation Results and Analysis

The Cartesian k-space data of the mineral oil phantom is displayed in Figure 2.2:

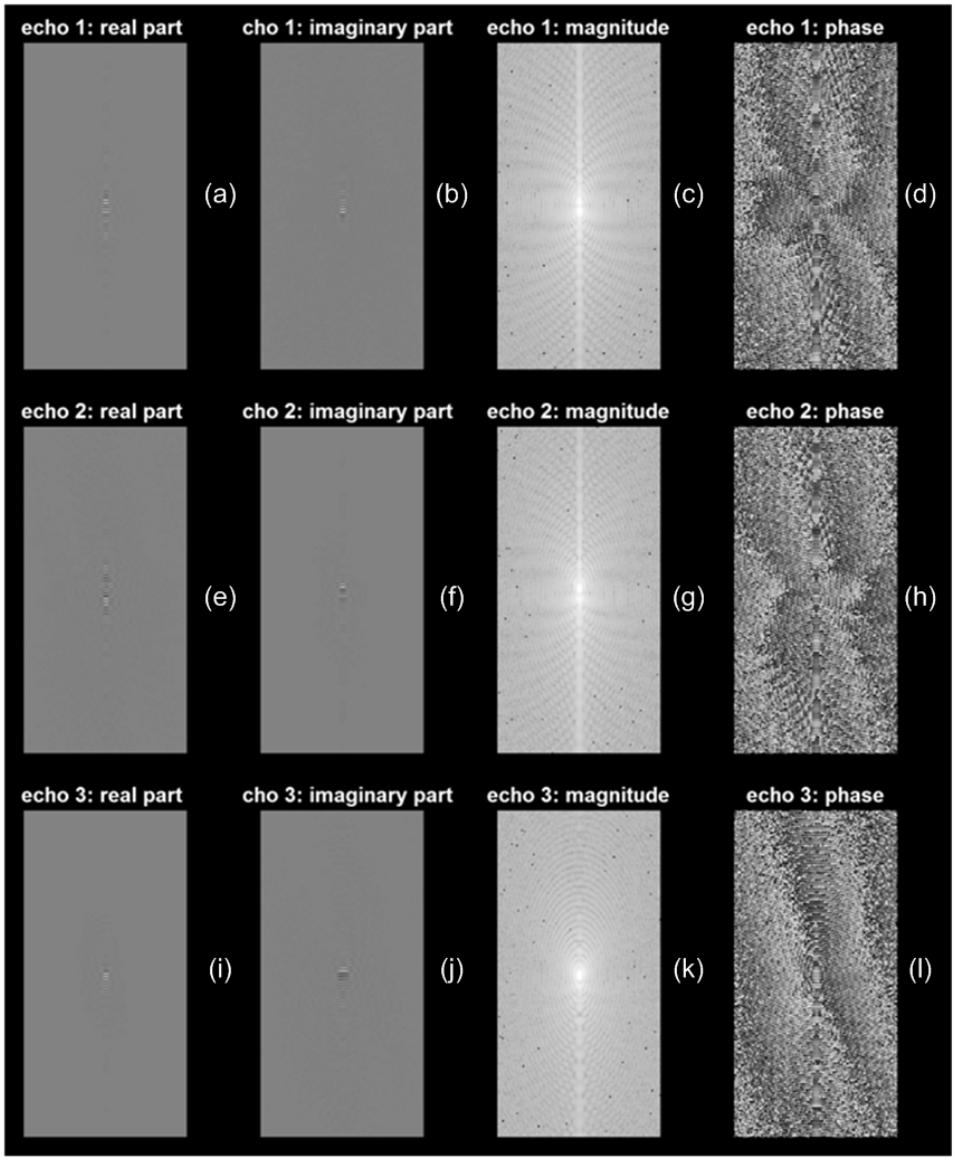

Figure 2.2. Mineral oil Cartesian k-space: Panel (a) through (d) are real part, imaginary part, magnitude and phase information for the first echo; Panel (e) through (h) are for second echo; Panel (i) through (l) are for the third echo.

Similarly, the Cartesian k-space data of peanut oil is shown in Figure 2.29:

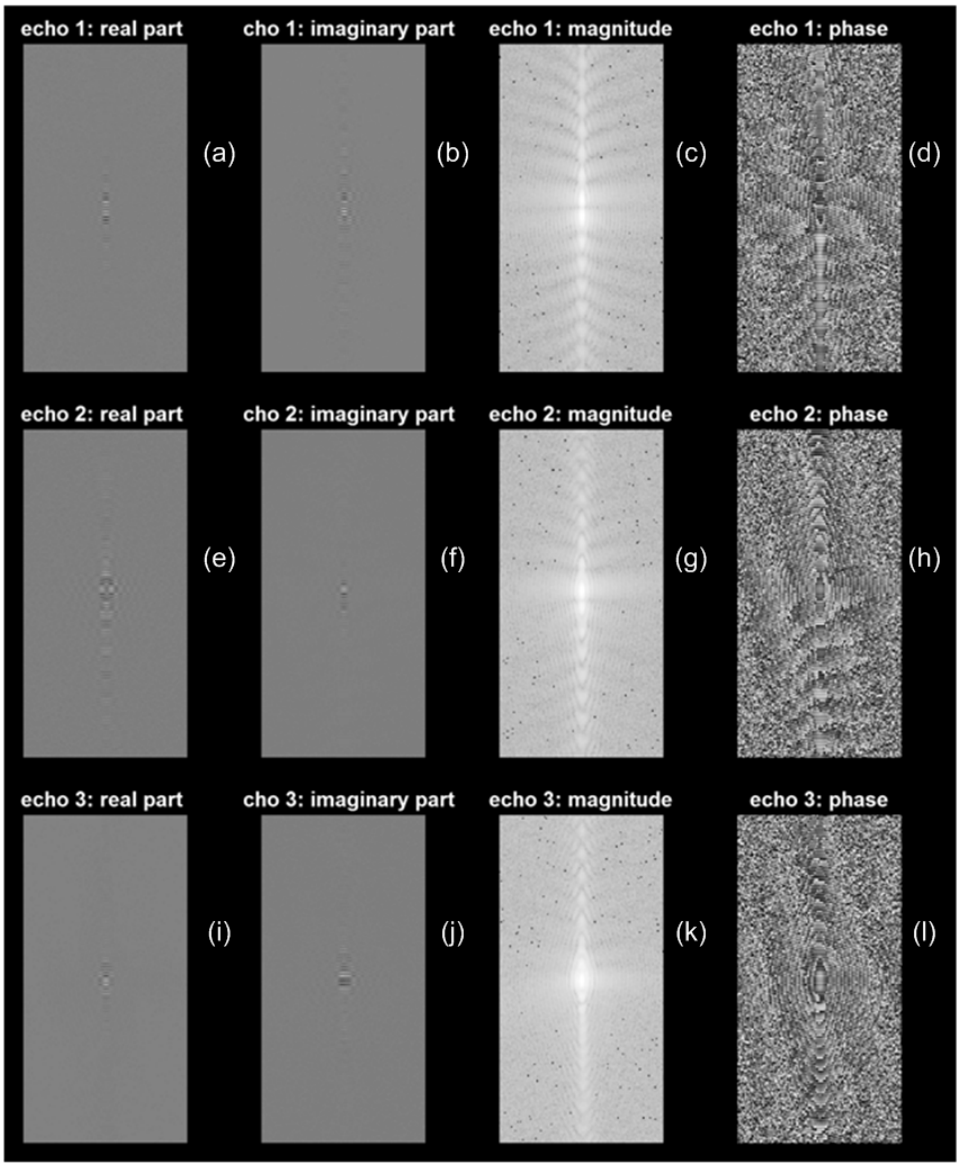

Figure 2.3. Peanut oil Cartesian k-space: Panel (a) through (d) are real part, imaginary part, magnitude and phase information for the first echo; Panel (e) through (h) are for second echo; Panel (i) through (l) are for the third echo.

For both phantoms, three echoes of data were collected.

Figure 2.3 shows the real part, imaginary part, the magnitude and the phase information of the mineral oil phantom across all the echo times. Due to T_2^* effect, slight signal drops can be

observed in the real part of the signal. However, the acquisition readout had a short duration, which created negligible T_2^* degradation:

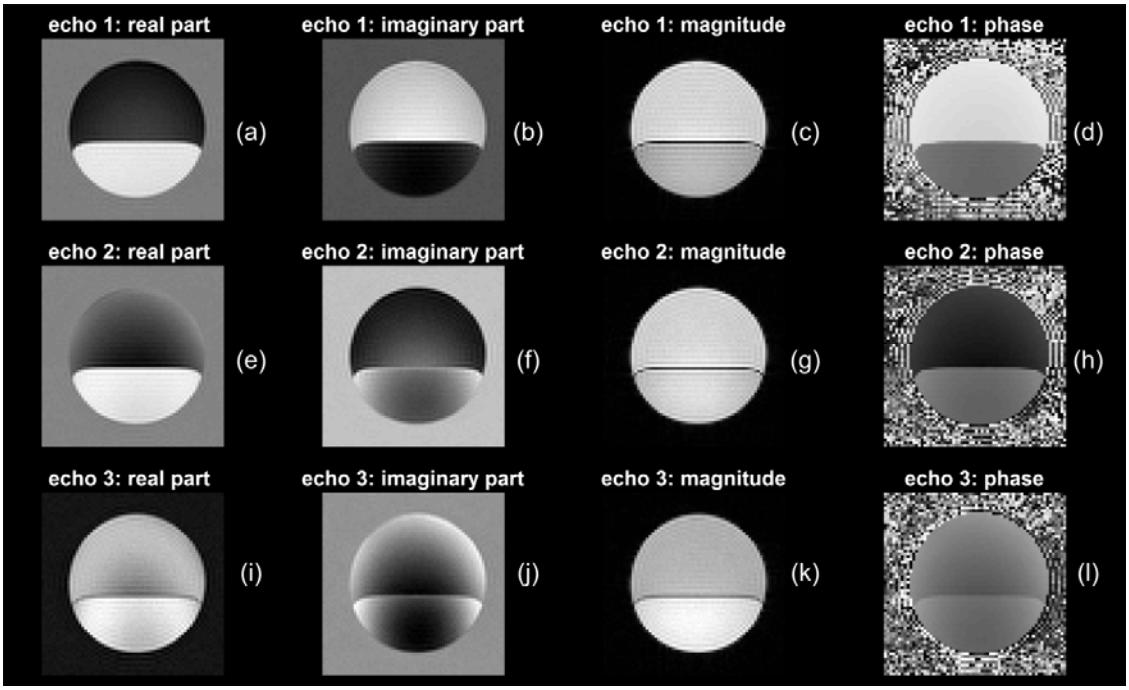

Figure 2.4. Mineral oil Cartesian reconstruction: Panel (a) through (d) are real part imaginary part, magnitude and phase information for the first echo, Panel (e) through (h) are for the second echo; Panel (i) through (l) are for the third echo.

Similarly, Figure 2.5 shows the real part, the imaginary part, the magnitude and the phase information for the peanut oild phantom across all the echo times:

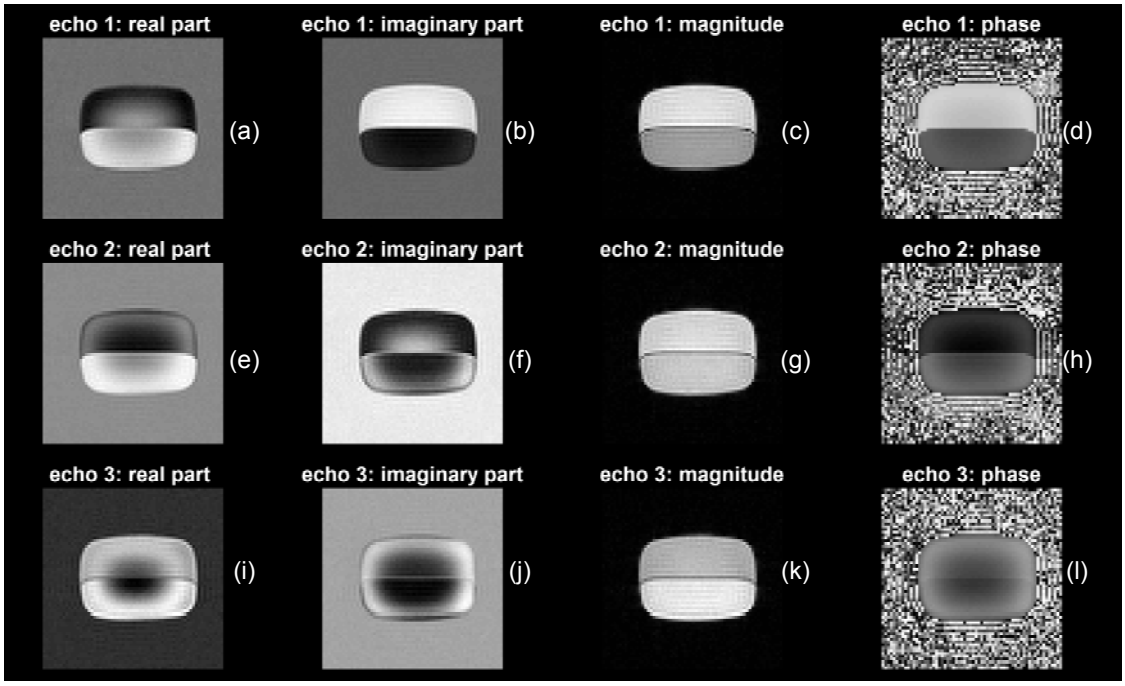

Figure 2.5. The peanut oil phantom Cartesian reconstruction: Panel (a) through (d) are real part imaginary part, magnitude and phase information for the first echo, Panel (e) through (h) are for the second echo; Panel (i) through (l) are for the third echo.

Before processing Cartesian k-space fat-water data, knowledge of field inhomogeneity map is needed since it impacts both fat and water signals within any voxel. The field inhomogeneity map is estimated using the IDEAL algorithm [15] which iteratively estimates the true value of the filed map at each spatial location in the image domain. The algorithm starts with an initial guess of the field map, typically zero, and then it explicitly updates the fat-water estimates at each iteration based on the new field map information just estimated. The stop criterion in this work was set 1 Hz as the change of field map magnitude between two consecutive iterations. A mask was created such that the background region is treated excluded. The filed map magnitude is measured in the unit of Hertz. The detailed algorithm for field map estimate for Cartesian data is explained in [15] and also previously in this work. Figure 2.6 shows the field inhomogeneity of the Cartesian mineral oil phantom data:

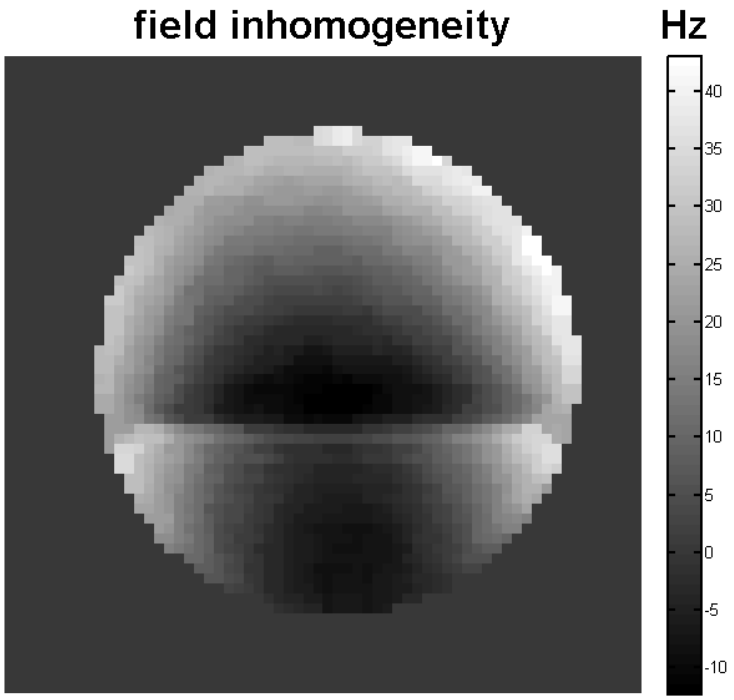

Figure 2.6. Estimated field inhomogeneity map for Cartesian mineral oil data using IDEAL method.

In Figure 2.6, it can be observed that there is a gap along the interface between water (bottom layer) and fat (top layer). Frequency from fat side rises about 50 Hz across the border to the water side. On the other hand, the field inhomogeneity map behaves as a spatially slowly varying function with dark regions representing low frequency and light regions corresponding to high frequency. The range of the field inhomogeneity is about 60 Hz. On the other hand, we do not see fat frequency offset (about 440 Hz) in this field inhomogeneity map, which shows the acquisition is short enough to avoid phase wrapping problem from occurring.

Likewise, Figure 2.7 shows the field inhomogeneity map for the peanut oil phantom solved by the IDEAL method:

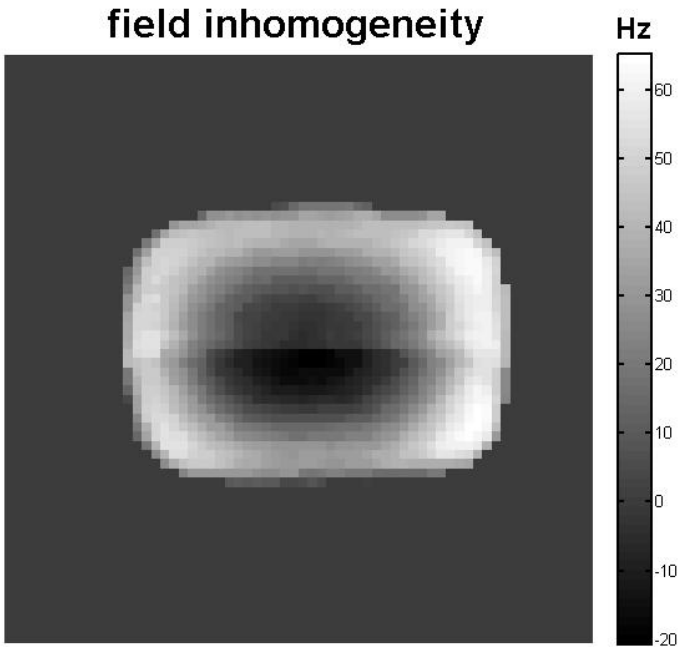

Figure 2.7. Estimated field inhomogeneity map for Cartesian peanut oil data using IDEAL method.

The estimated field inhomogeneity map for the peanut oil phantom also changes smoothly across the FOV. It behaves as a bowl-shaped function with central portion lower than the edges. The total range of the field map variation is about 80 Hz.

Aside from the field inhomogeneity map, another factor considered in this work is the time point at which each sample in k-space is acquired. This requires information from two sources: first, the center of each echo time; second, $\tau_{k,n}$, the time delay from the center of the echo

time for each k-space sampling location. The centers of echo time for our Cartesian experiment are 1.3402 ms, 2.9902 ms and 4.6402 ms, and it is known that the acquisition time for each echo is 0.7461 ms. So it is straightforward to conclude that the $\tau_{k,n}$ ranges from -0.37305 ms to 0.37305 ms as illustrated in Figure 2.8:

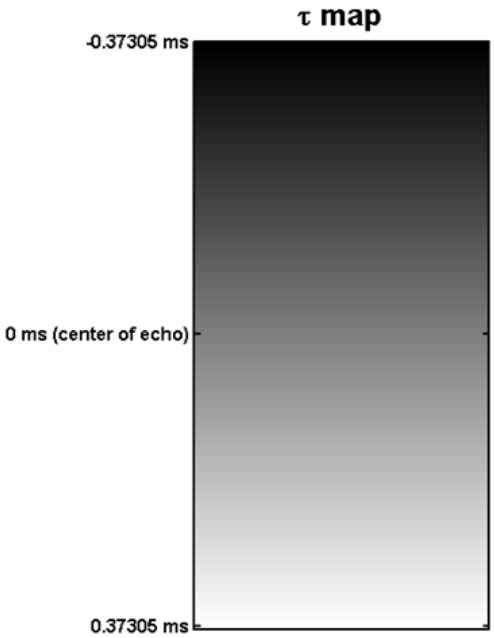

Figure 2.8. $\tau_{k,n}$ map showing sampling time lag, ranging from -0.37305ms to 0.37305ms, compared to the center of the k-space.

It should be pointed out that the mineral oil phantom and the peanut oil phantom share same $\tau_{k,n}$ map because both were acquired using the same pulse sequence.

The final reconstruction is formed after field inhomogeneity and chemical shift effects are corrected. Figure 2.9 shows the fat-water separation for the Cartesian mineral oil phantom:

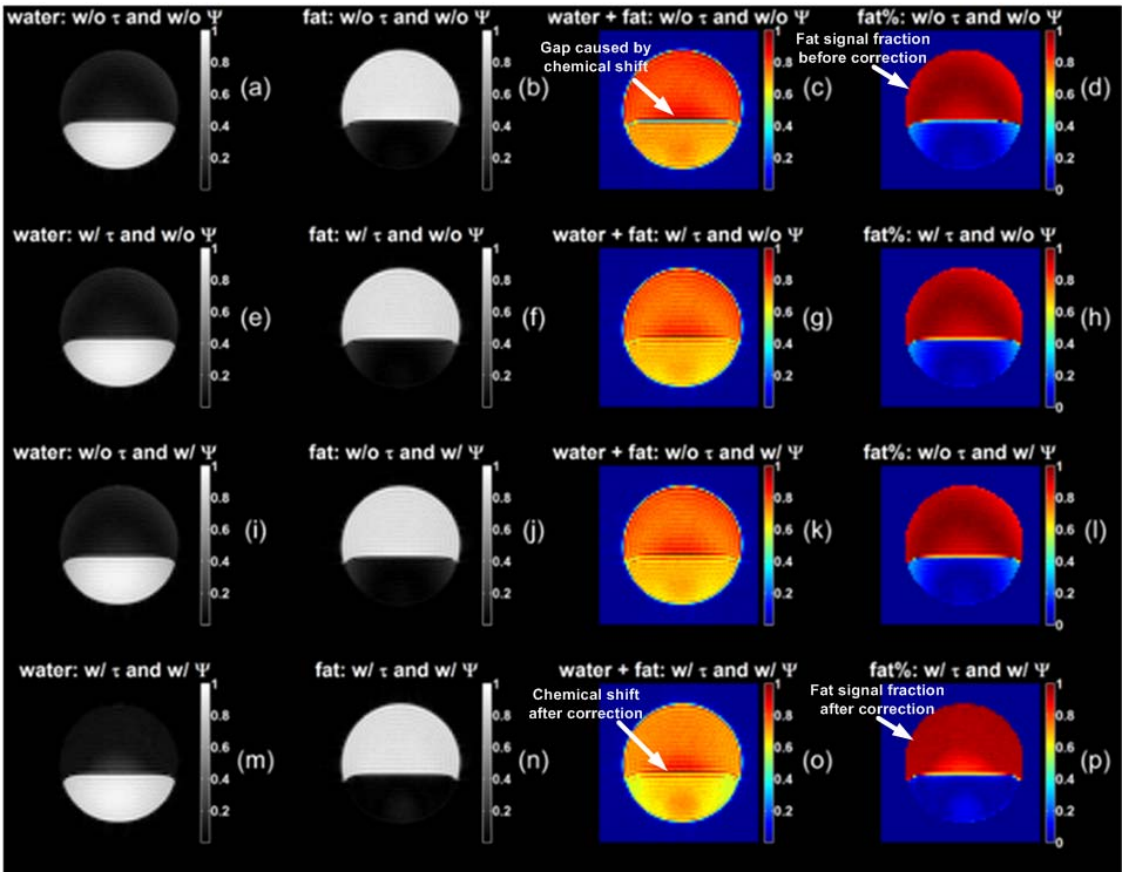

Figure 2.9. Mineral oil fat-water separation results from a Cartesian acquisition: Panel (a) through (d) is water signal, fat signal, summation of fat and water signal, and fat signal percentage when there is neither $\tau_{k,n}$ map correction nor field inhomogeneity correction. Panel (e) through (h) is water signal, fat signal, summation of fat and water signal, and fat signal percentage when there is $\tau_{k,n}$ map correction but no field inhomogeneity correction. Panel (i) through (l) is water signal, fat signal, summation of fat and water signal, and fat signal percentage when there is no $\tau_{k,n}$ map correction but field inhomogeneity correction. Panel (e) through (h) is water signal, fat signal, summation of fat and water signal, and fat signal percentage with both $\tau_{k,n}$ map correction but and field inhomogeneity correction.

It can be observed in Figure 2.9, especially via fat signal percentage (panel (d) through (p) from top to bottom), that improvement occurs in fat signal percentage when $\tau_{k,n}$ map correction and field inhomogeneity correction are both applied. Panel (p) shows a higher fat signal fraction, particularly in the top area of the phantom, than its three equivalents from

panel (d) to panel (i) vertically. On the other hand, the chemical shift can be observed in panel (c), where a gap exists between fat and water along their interface. This displacement, caused by chemical shift artifact, is corrected in panel (g) through panel (o) with panel (o) giving the best result when both $\tau_{k,n}$ map and field inhomogeneity artifacts are corrected. Performance of fat-water separation is measured by observing the average fat signal fraction for each fat pixel. The fat signal fraction is listed in Table 2.1:

Table 2.1. Fat signal percentage with different corrections for the Cartesian mineral oil phantom.

corrections	w/o $\tau_{k,n}$; w/o ψ	w/ $\tau_{k,n}$; w/o ψ	w/o $\tau_{k,n}$; w/ ψ	w/ $\tau_{k,n}$; w/ ψ
Fat Signal Percentage	88.44%	89.00%	89.69%	90.35%

From Table 2.1, it can be seen that field inhomogeneity correction is a more dominant factor in fat-water signal reconstruction than $\tau_{k,n}$ map correction. The fat signal fraction increases from 88.44% to 89.00% suggests that $\tau_{k,n}$ correction might have limited effect in reconstruction process especially when readout duration is short. On the other hand, the fat signal fraction improves from 88.44% to 89.69% due to field inhomogeneity correction. However, when both field inhomogeneity correction and $\tau_{k,n}$ correction are applied, the fat signal percentage increases from 84.55% to 90.35%, which is the best result compared to either correction individually.

Figure 2.10 shows chemical shift correction seen as 1D profile. It shows the comparison between uncorrected and corrected data. Adjustments include both the $\tau_{k,n}$ map correction and the field inhomogeneity correction:

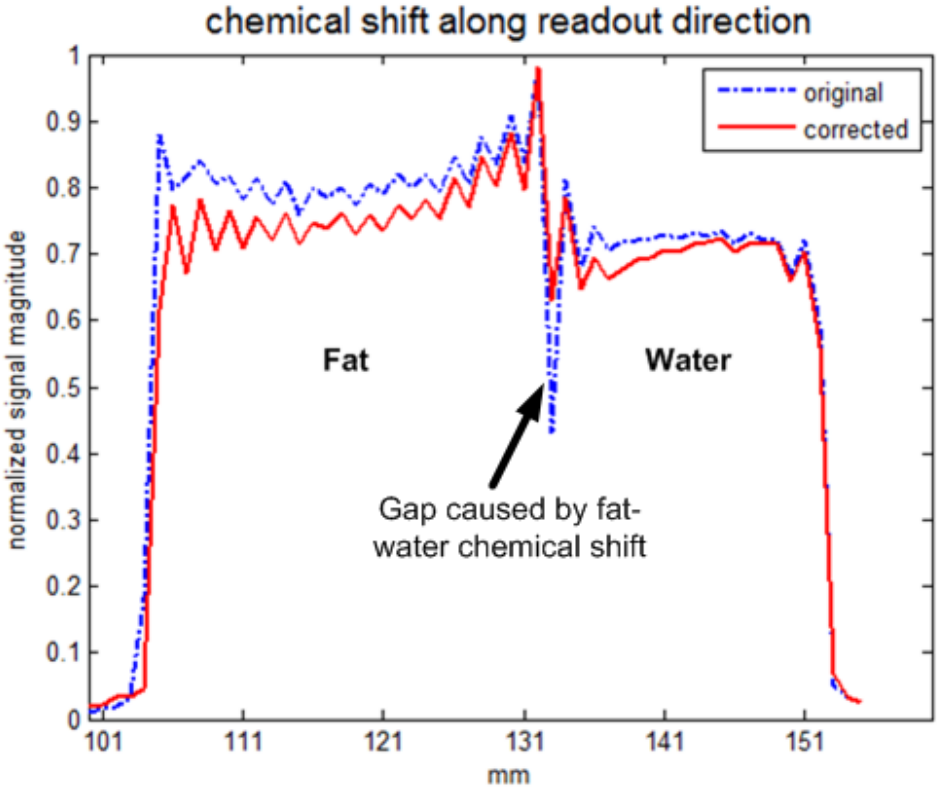

Figure 2.10. A gap caused by chemical shift between fat and water in the mineral oil phantom depicted by blue dotted curve is corrected in red curve in which both the field inhomogeneity and the chemical shift are corrected.

Figure 2.11 shows the final fat-water separation for the Cartesian peanut oil data:

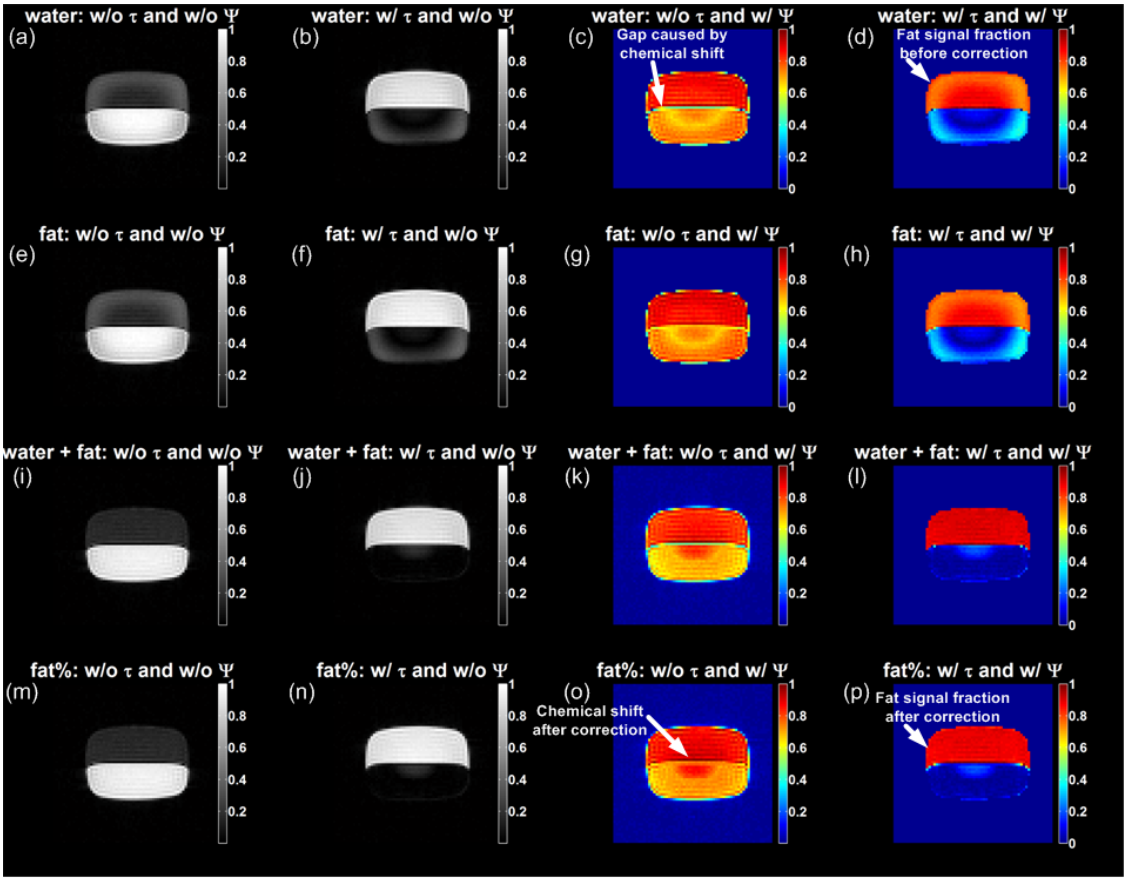

Figure 2.11. Peanut oil fat-water separation results from a Cartesian acquisition: Panel (a) through (d) is water signal, fat signal, summation of fat and water signal, and fat signal percentage when there is neither $\tau_{k,n}$ map correction nor field inhomogeneity correction. Panel (e) through (h) is water signal, fat signal, summation of fat and water signal, and fat signal percentage when there is $\tau_{k,n}$ map correction but no field inhomogeneity correction. Panel (i) through (l) is water signal, fat signal, summation of fat and water signal, and fat signal percentage when there is no $\tau_{k,n}$ map correction but field inhomogeneity correction. Panel (e) through (h) is water signal, fat signal, summation of fat and water signal, and fat signal percentage with both $\tau_{k,n}$ map correction but and field inhomogeneity correction.

Compared to the fat-water separation the results of the mineral oil phantom, the peanut oil phantom substantiate the robustness of the separation technique. For example, it is clear to see the enhancement of fat signal fraction in the mineral oil phantom when one compares

panel (d) with panel (p). The improvement in fat signal percentage with different corrections is listed in Table 2.2:

Table 2.2. Fat signal percentage with different corrections for the Cartesian peanut oil phantom.

corrections	w/o $\tau_{k,n}$; w/o ψ	w/ $\tau_{k,n}$; w/o ψ	w/o $\tau_{k,n}$; w/ ψ	w/ $\tau_{k,n}$; w/ ψ
Fat Signal Percentage	79.17%	79.14%	84.36%	84.53%

Table 2.2 also confirms that field inhomogeneity correction has more significant impact on the quality of fat-water separation. Although fat signal percentage decreases a small portion when only $\tau_{k,n}$ map correction is applied, the fat signal percentage has its maximum value when both field inhomogeneity and $\tau_{k,n}$ map correction are performed. It should also be emphasized that the gap between fat and water in panel (c) also disappears in panel (o) due to $\tau_{k,n}$ map correction.

This example also shows the importance of using two phantoms instead of one. Compared to the mineral oil phantom, the peanut oil phantom is more sensitive to the underlying field inhomogeneity, which makes the field inhomogeneity correction contributes more improvement in signal reconstruction than the mineral phantom.

Likewise, the gap along the fat water interface is mitigated in Figure 2.12:

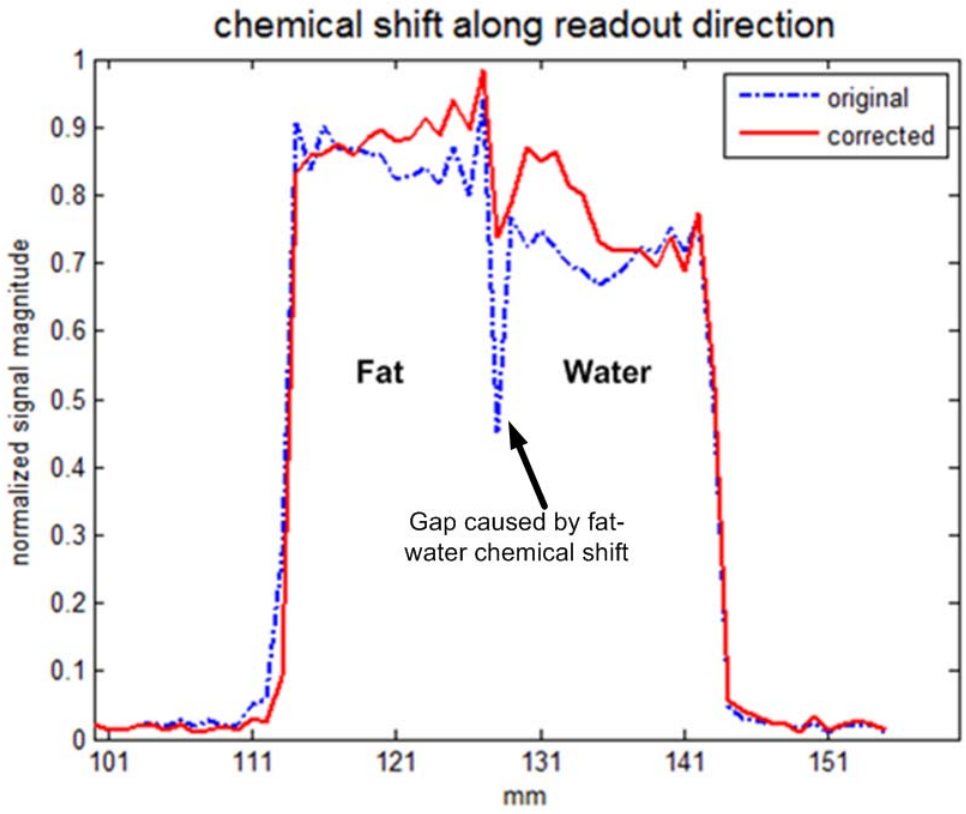

Figure 2.12. A gap caused by chemical shift between fat and water in the peanut oil phantom depicted by blue dotted curve is corrected in red curve in which both the field inhomogeneity and the chemical shift are corrected.

In Figure 2.11, the blue curve shows the profile of the reconstructed fat-water image for peanut oil phantom along its midline vertically. It can be seen that after correction for field inhomogeneity and chemical shift, the gap rises significantly in the red curve compared to that in blue curve.

The results show that the IDEAL method is a feasible way to correct image degradation caused by the field inhomogeneity, but the method proposed by Brodsky in 2008 [16] extended IDEAL fat-water signal separation by adding $\tau_{n,k}$ map correction. Further processing, which corrects data corruption associated with the time point at which one

location is sampled, is performed in k-space. Experimental results show that the IDEAL method combined with Brodsky's method [16] is an effective procedure to perform Cartesian fat-water data separation.

2.5 Results of Radial Fat-Water Separation

Single channel MRI data, both Cartesian and radial, of a set of phantoms were acquired on a 3T Achieva scanner (Philips Healthcare, Best, The Netherlands). The same phantoms, one mineral oil phantom and one peanut oil phantom, were used for both the Cartesian and the radial trajectories.

2.5.1 Data Collection

Radial k-space data were acquired using a radial sampling scheme of 201 projections equally spaced over 180° on a 3T Achieva MRI scanner (Philips Healthcare, Best, The Netherlands). Data were acquired with alternating frequency encode (readout) direction as illustrated in Figure 2.12. The same phantoms, mineral oil phantom and peanut phantom, were scanned as previously discussed. Field of view (FOV) was 256 mm$\times$256 mm with 256 readout samplings evenly distributed symmetrically about DC ($k_x = 0, k_y = 0$) along each projection. Bandwidth (BW) in readout direction is 1.3403 kHz/pixel, which in turn made readout duration 0.7461 ms. Data were acquired with time of repetition (TR) equal to 75 ms and at 3 echo times centered at 1.3402 ms, 2.9902 ms and 4.6402 ms, respectively. Two dynamics of data were scanned, to calculate SNR, with each dynamic consisting of 12 slices. In addition to the fat-water phantoms, a Philips picture imaging quality test (PIQT) phantom was also used to evaluate the correction.

2.5.2 Alternating Frequency Encoding Correction

As mentioned previously, the radial MRI data were sampled with readout direction changing in an alternating pattern. A primary challenge associated with this sampling strategy is the imperfect alignment of each sampled diagonal with the center of k-space. Gradient imperfections and timing delay errors cause the sampled trajectory to shift from the intended trajectory [17]. The shift changes as the readout direction is rotated. The opposite readout direction causes the shift to be in opposite directions as also illustrated in Figure 2.13:

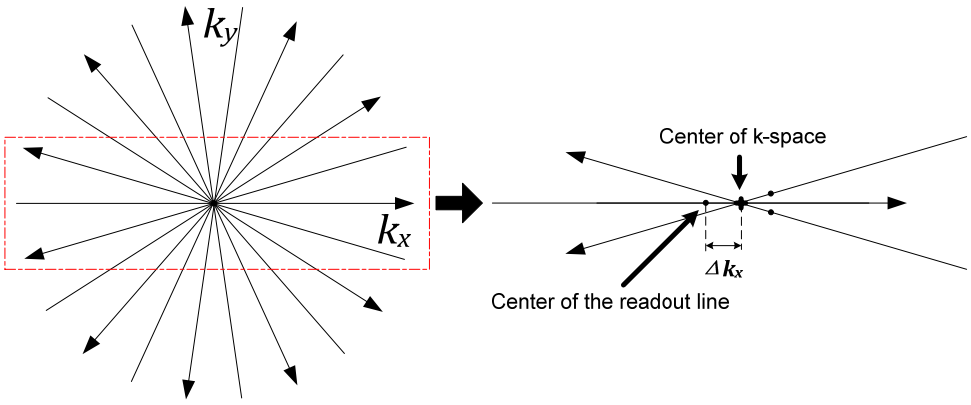

Figure 2.13. Left part of the figure shows the radial sampling trajectory. On the right is an exaggerated explanation of the red window. The center of each readout line, the bold black dot, is shifted away from the center of the k-space by Δk_x.

Prior to image reconstruction, the alternating readout direction artifact needs to be corrected. In particular, the artifact is caused by the shift occurring in k-space, so the correction aims at removing the undesired shift in k-space such that all projections are exactly lined up at the center of the k-space.

According to the Fourier Shift theorem, translation in one domain corresponds to a linear phase shift in the other domain. In this case, the shift artifact exists in k-space, so it is equivalent to perform complex multiplication in the spatial domain. This suggests the artifact

of k-space center misplacement can be compensated by phase correction in the spatial domain. The shift to be corrected is illustrated in Figure 2.12 depicted as Δk_x, and it is assumed that the alternating shift artifact happens symmetrically around the center of the k-space.

In this work, directly solving for Δk_x is not straightforward since the location of the center of the k-space is unknown. Instead, $2\Delta k_x$ was estimated rather than solving Δk_x directly, To do that, a projection acquired with opposite readout gradient is needed. As described previously, over 200 projections are evenly sampled across $180°$ (201 for the fat-water phantoms, and 256 for the PIQT phantom), so it is reasonable to make following approximation: For the nth readout in radial k-space, its reversed gradient approximation can be estimated by averaging its two nearest neighbors. We assume that readout lines sampled with reversed readout gradient should have same amount of shift from the center of the k-space, and the amount of shift about the center of the k-space is symmetrical. The total shift between the original projection and its reversed should be $2\Delta k_x$.This is illustrated in Figure 2.14:

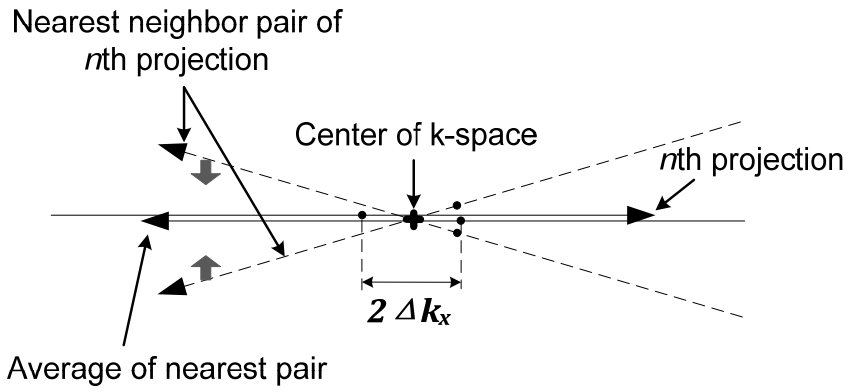

Figure 2.14. The shift between n th projection and its reversed readout approximation is $2\Delta k_x$

The phase change in the spatial domain caused by the misalignment shift $2\Delta k_x$ in k-space along a single projection can be written as following:

$$S(k + 2\Delta k_x) = F\left\{s(x)e^{j2\pi x(2\Delta k_x)}\right\} \quad 2.27$$

where $F\{\cdot\}$ is the Fourier transform operator, and $S(k)$ is the Fourier transform of $s(x)$.

Inverse Fourier transformation of each projection in k-space produces spatial projections arranged as a sinogram. For each single projection in sinogram space, the oppositely shifted projection is approximated using the average of the nearest neighbors. The complex exponential terms $e^{i2\pi x(2\Delta k_x)}$ can then be computed by taking the ratio of the original projection line to its approximation with opposite shift. The phase terms, $2\pi x(2\Delta k_x)$, are therefore straightforward to calculate as follows. It can be seen that the phase terms behave as a linear function of position in the spatial domain along the projection, and $2\Delta k_x$ is the slope of the linear function. A matrix representation describing the relation between the positions and parameters is shown in Equation 2.28:

$$\begin{bmatrix} y_1 \\ y_2 \\ \vdots \\ y_4 \end{bmatrix} = \begin{bmatrix} 1 & x_1 \\ 1 & x_2 \\ \vdots & \vdots \\ 1 & x_4 \end{bmatrix} \begin{bmatrix} m \\ b \end{bmatrix} + \begin{bmatrix} \varepsilon_1 \\ \varepsilon_2 \\ \vdots \\ \varepsilon_4 \end{bmatrix}, \quad 2.28$$

where, y_n is the phase at nth position x_n, x_n is nth position along projection direction, m and b are the slope and intercept, respectively, and ε_n is the noise. A simplified format can be written as:

$$Y = XA + E. \quad 2.29$$

The estimate of A, based on least square criterion, is

$$\hat{A} = \left(X^T W X\right)^{-1} X^T W Y, \qquad 2.30$$

where $\hat{m}$ is the first element of $\hat{A}$, and W is a diagonal matrix that treats anything less than 10% of the signal peak as noise

In this application, only the slope information is related to Δk_x, and there is no further use of intercept information. Figure 2.15 shows the linear estimate of the phase difference in the spatial domain:

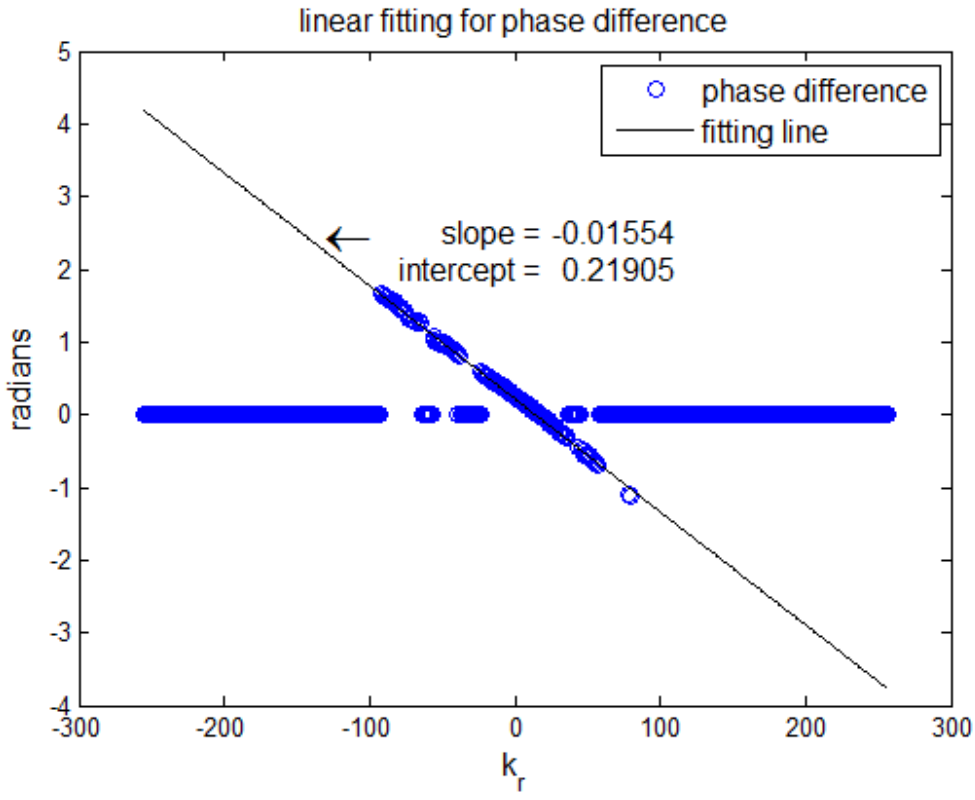

Figure 2.15. The linear fitting for phase difference between a spatial domain projection and its reversed approximation.

Figure 2.15 shows an example of linear fitting for one single projection. The blue circles indicate the phase difference as a function of position. The black solid the line is the fit based on the least square approach described above.

The linear fitting solves the slope and intercept, and only the slope information is needed for Δx_k estimate. After Δx_k correction for k-space shift artifact also takes place in spatial domain. Each projection with Δx_k displacement in k-space is multiplied by a phase corrector $e^{j2\pi x\left(-\Delta k_x\right)}$. The corrected radial k-space of the PIQT phantom is shown in Figure 2.16:

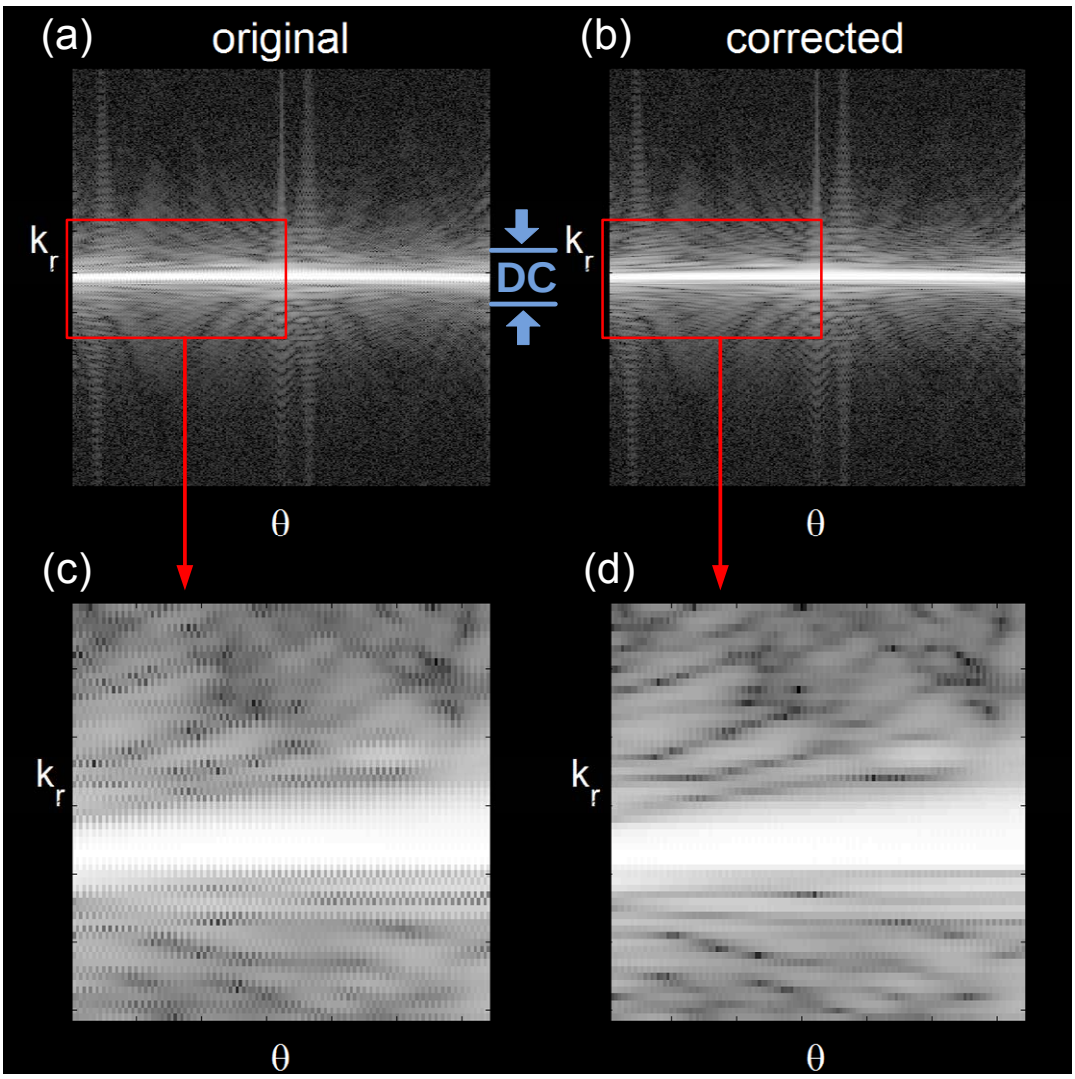

Figure 2.16. Comparison between original (panel (a)) and corrected (panel (b)) radial k-space of PIQT phantom. Zoom-in of the highlighted area is displayed in panel (c) and panel (d).

Panel (a) shows the radial k-space data without any correction. The highlighted area is shown in panel (c) where a sawtooth pattern is clearly displayed around direct DC ($k_r = 0$) area. Panel (b) shows corrected radial k-space data with apparent improvement, for example better smoothness, around DC area. The zoom-in of highlighted area in panel (b) is shown as panel (d). Figure 2.17 shows the sinogram of original and corrected k-space:

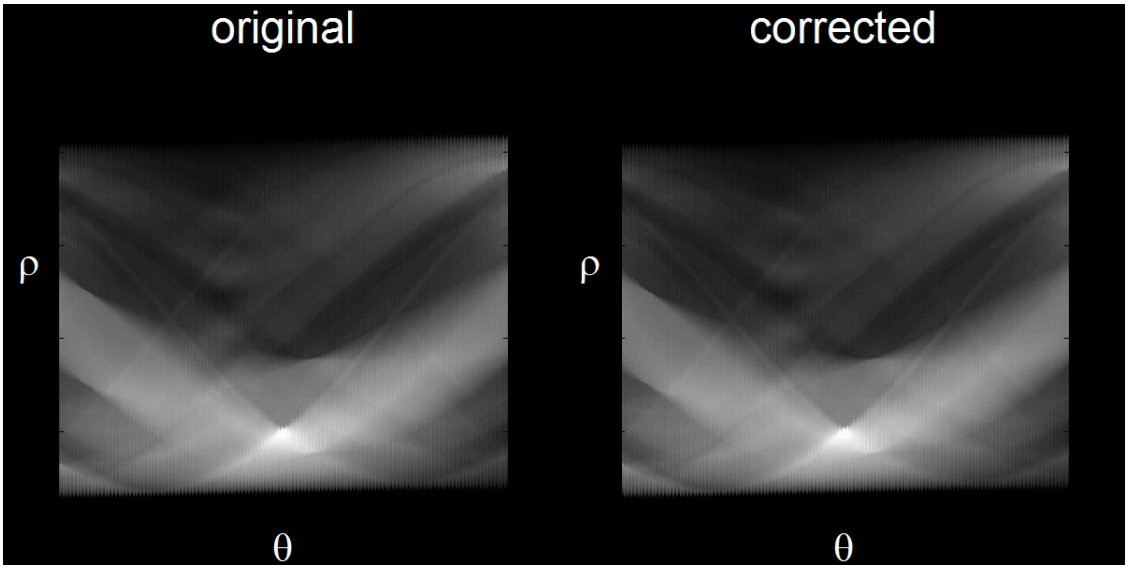

Figure 2.17. Comparison between sinogram from original k-space data on the left and sinogram from corrected k-space data on the right.

Unlike the noticeable difference in k-space, there is nearly no change visible in the sinogram as shown in Figure 2.17. This is because only phase correction is applied to sinogram, which means only “phasors” are multiplied with sinogram data.

Reconstruction is completed using NUFFT [18] toolbox developed by Fessler. Results are compared between the original k-space data and the corrected k-space data. Signal to noise ratio (SNR) is also calculated by taking the ratio of the signal within the orange highlight against the noise from green highlight. The illustration is shown in Figure 2.18 below:

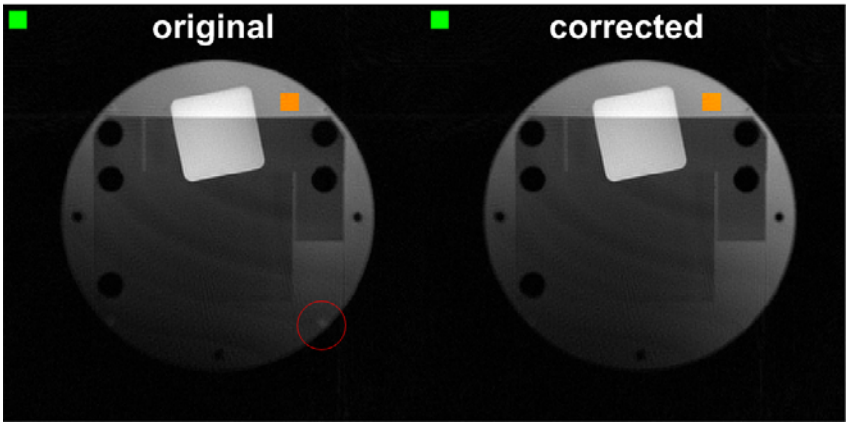

Figure 2.18. Improvement is observable within red circle with white spot inside removed.

The SNR in left panel is increased from 58.2 to 58.5 in right panel. Similarly, SNR defined as signal from the yellow ROI to noise from the green ROI improves from 0.55 to 0.60. This is shown in Figure 2.19:

Figure 2.19. SNR improvements in fat-water phantom after k-space misalignment correction.

2.5.3 Separation Results and Analysis

Like Cartesian results that are shown in previous section, separation results for radial MRI fat-water data are also displayed with k-space data, reconstructed image, $\tau_{n,k}$ map, field

inhomogeneity map, as well as fat signal fraction. Figure 2.20 shows the radial k-space data of mineral oil phantom:

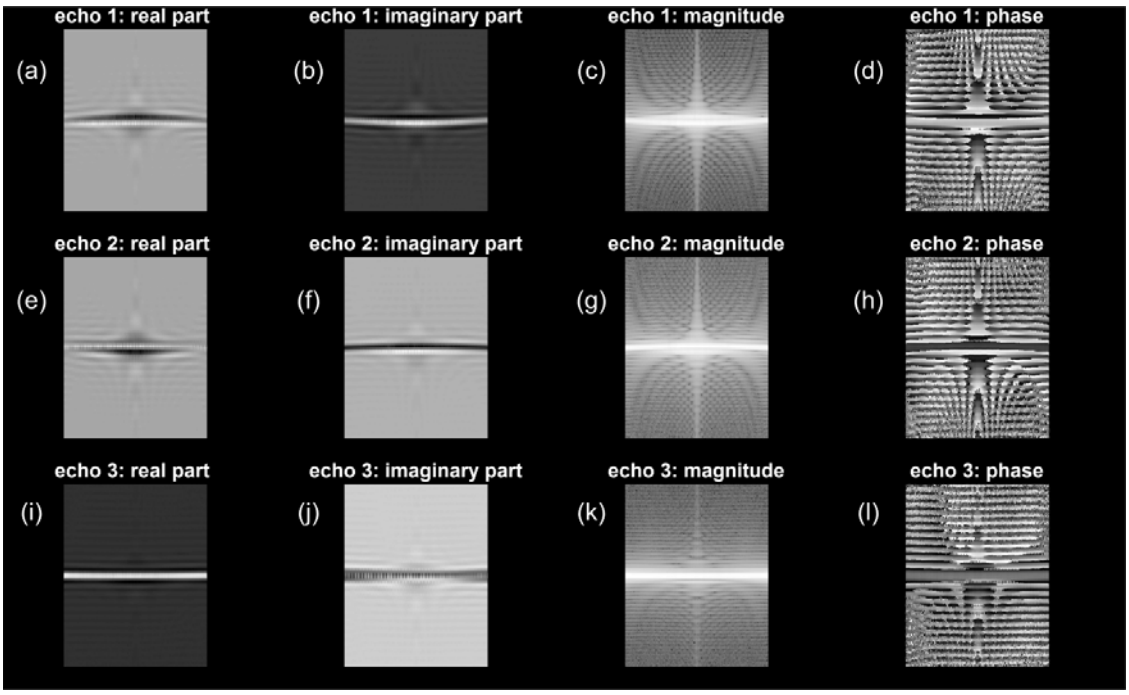

Figure 2.20. The mineral oil phantom radial k-space: Panel (a) through (d) are real part, imaginary part, magnitude and phase information for the first echo; Panel (e) through (h) are for second echo; Panel (i) through (l) are for the third echo.

It should be mentioned that the magnitude displayed in Figure 2.20 is based on a log scale.

Figure 2.21 below displays the image reconstruction results of radial mineral oil data:

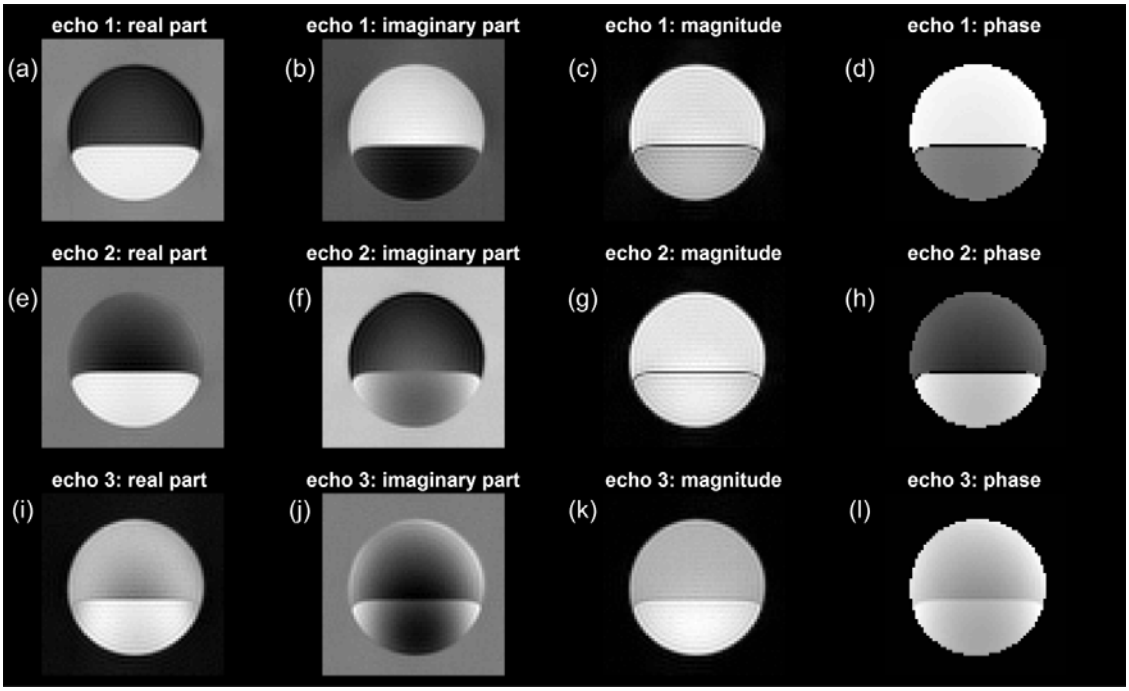

Figure 2.21. The mineral oil phantom radial reconstruction: Panel (a) through (d) are real part imaginary , magnitude and phase information for the first echo, Panel (e) through (h) are for the second echo; Panel (i) through (l) are for the third echo.

Figure 2.22 and 2.23 show the results for the peanut oil phantom. The radial k-space data are

displayed in Figure 2.22, and the reconstructed image data are demonstrated in Figure 2.23.

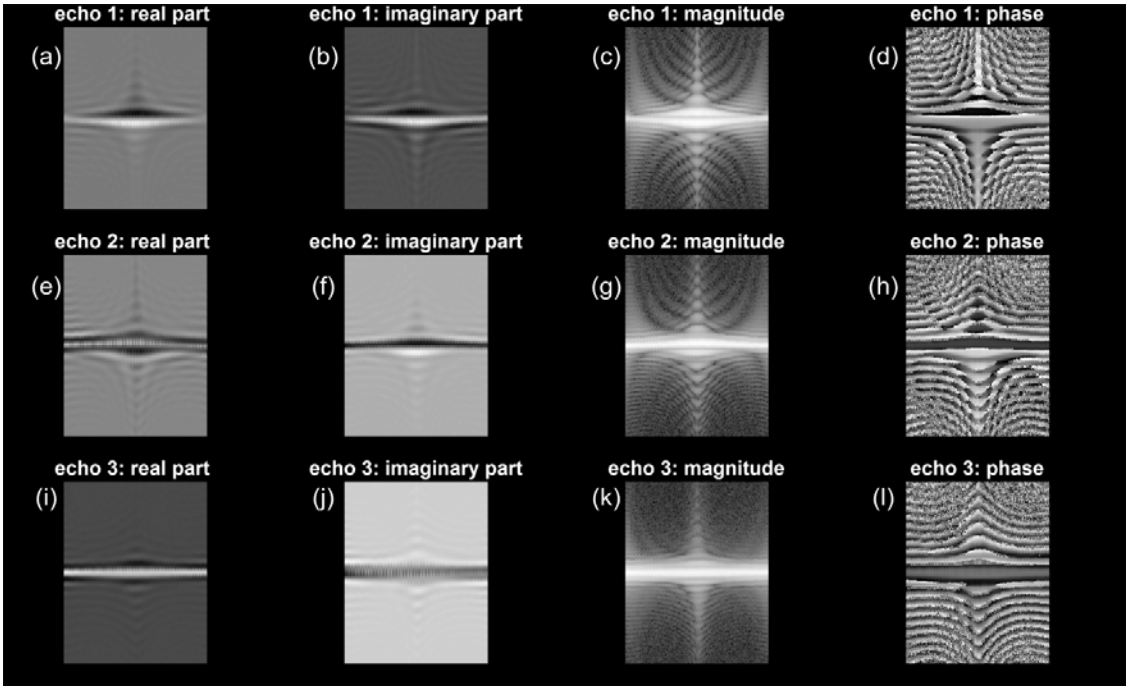

Figure 2.22. The peanut oil radial k-space: Panel (a) through (d) are real part, imaginary part, magnitude and phase information for the first echo; Panel (e) through (h) are for second echo; Panel (i) through (l) are for the third echo.

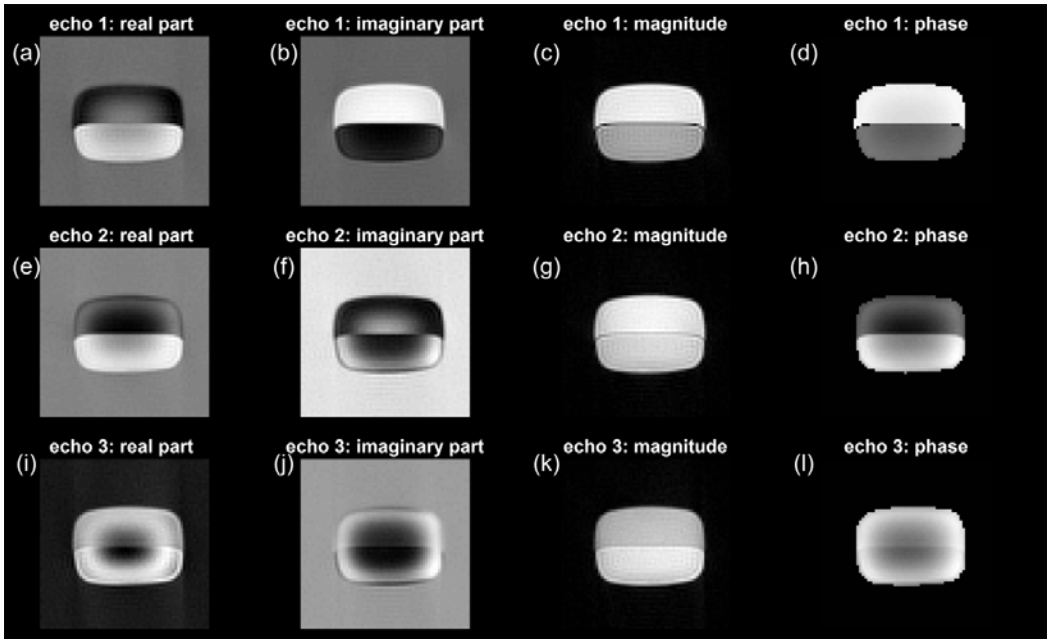

Figure 2.23. The peanut oil phantom radial reconstruction: Panel (a) through (d) are real part imaginary , magnitude and phase information for the first echo, Panel (e) through (h) are for the second echo; Panel (i) through (l) are for the third echo.

$\tau_{n,k}$ map is shown in Figure 2.24:

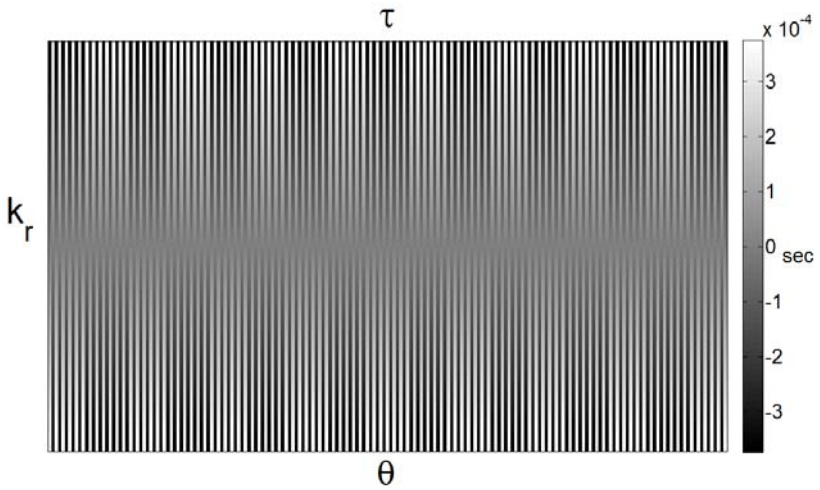

Figure 2.24. $\tau_{k,n}$ map for radial sampling scheme.

Both the mineral oil phantom and the peanut oil phantom share the same radial sampling

scheme, which is illustrated in Figure 2.24. The $\tau_{k,n}$ map is arranged in the same as raw k-space data. Each column is associated with a single projection in k-space.

The estimated field inhomogeneity map is similar to that estimated for the Cartesian acquisition, which is expected because the underlying field map nearly remains consistent. Therefore, the field map is very similar as Cartesian reconstruction. Because estimating field map for radial data is formidable, this work used the field map from the Cartesian estimate for radial data. For the mineral oil phantom, the filed map is displayed in Figure 2.25:

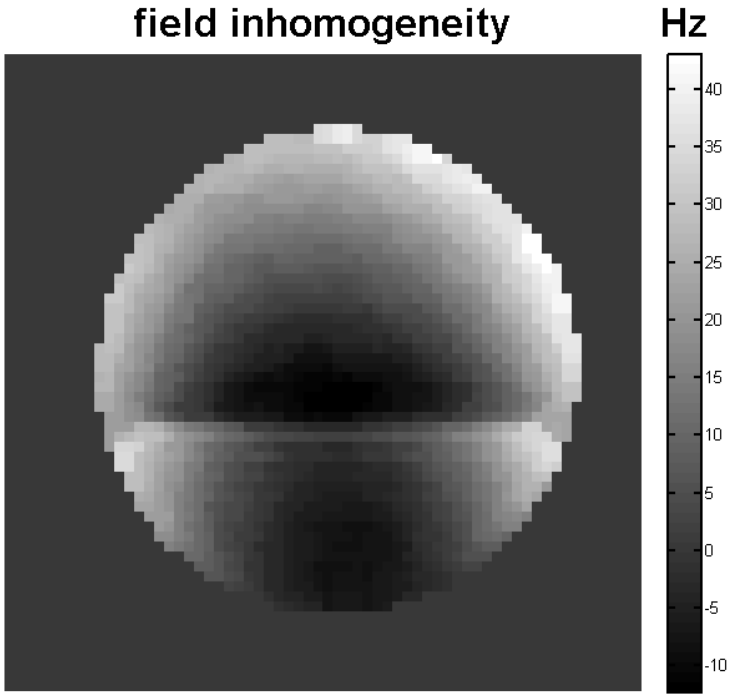

Figure 2.25. Estimated field inhomogeneity map for the mineral oil phantom.

For the peanut oil phantom the field map is shown in Figure 2.26:

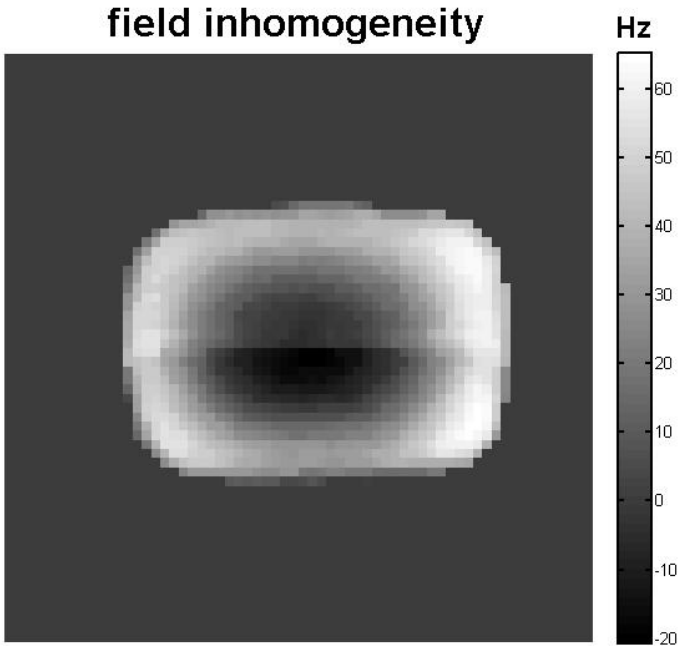

Figure 2.26. Estimated field inhomogeneity map for the peanut oil phantom.

Figure 2.27 shows separation results of mineral oil phantom. The fat signal fraction is an indicator of how effective the corrections are:

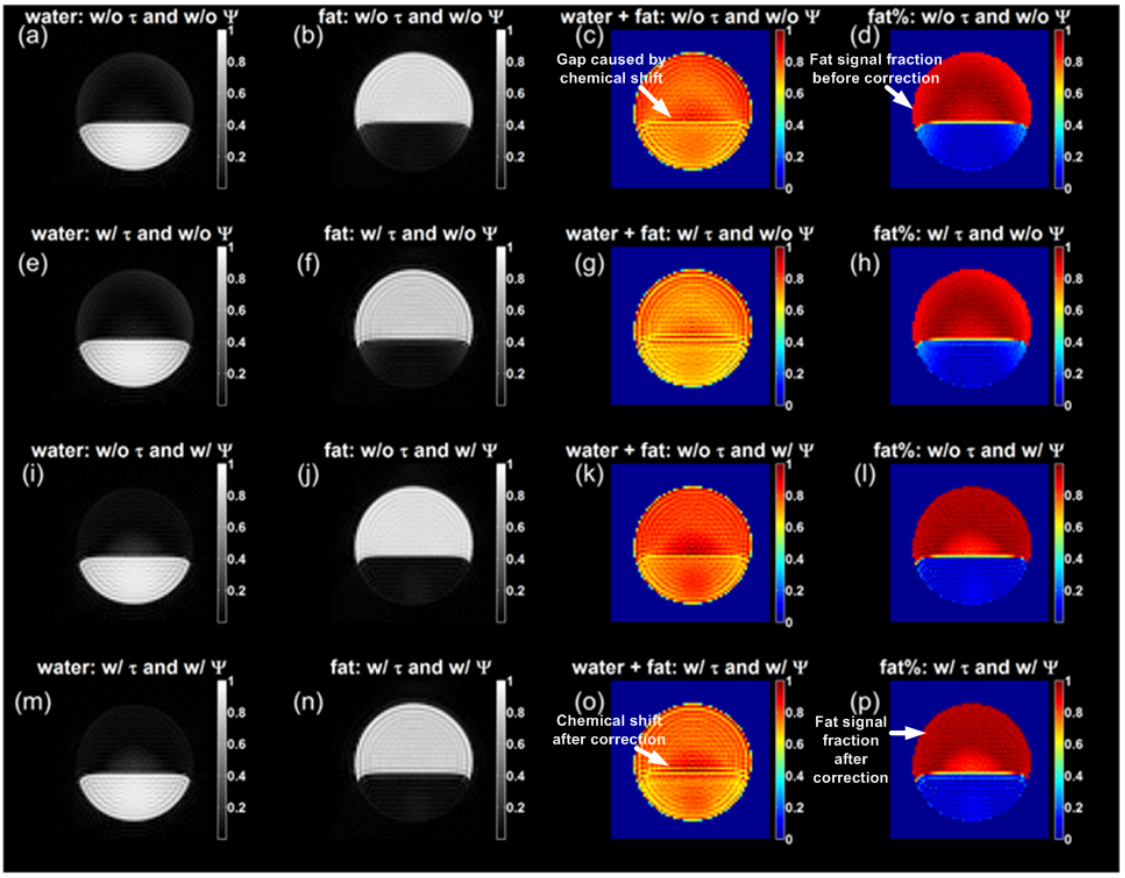

Figure 2.27. The Mineral oil fat-water separation results from a radial acquisition: Panel (a) through (d) is water signal, fat signal, summation of fat and water signal, and fat signal percentage when there is neither $\tau_{k,n}$ map correction nor field inhomogeneity correction. Panel (e) through (h) is water signal, fat signal, summation of fat and water signal, and fat signal percentage when there is $\tau_{k,n}$ map correction but no field inhomogeneity correction. Panel (i) through (l) is water signal, fat signal, summation of fat and water signal, and fat signal percentage when there is no $\tau_{k,n}$ map correction but field inhomogeneity correction. Panel (e) through (h) is water signal, fat signal, summation of fat and water signal, and fat signal percentage with both $\tau_{k,n}$ map correction but and field inhomogeneity correction.

Similar features can be observed for radial data separation. Panel (d) through (p) vertically demonstrate clear improvement in fat signal fraction as a precise separation indicator. Fat signal percentage becomes more realistic when $\tau_{k,n}$ map correction and field inhomogeneity correction are both involved in correction procedure. Panel (p) shows the best fat signal

percentage level amongst all. The fat signal fraction improvement increase more significantly when field map is applied than when $\tau_{k,n}$ map is applied. On the other hand, the chemical shift correction in radial case does not have as much improvement as in Cartesian case. The quantitative improvement due to each correction is listed in Table 2.3:

Table 2.3. Fat signal percentage with different corrections for the Cartesian mineral oil phantom.

corrections	w/o $\tau_{k,n}$; w/o ψ	w/ $\tau_{k,n}$; w/o ψ	w/o $\tau_{k,n}$; w/ ψ	w/ $\tau_{k,n}$; w/ ψ
Fat Signal Percentage	91.60%	92.96%	91.66%	93.02%

It can be seen from Table 2.3 that each individual correction contributes to signal reconstruction quality. Although signal strength increases less when only field inhomogeneity correction is applied than when only $\tau_{k,n}$ correction is applied, there is no significant difference in signal strength improvement. The fat signal percentage improves to it maximum value when both field inhomogeneity correction and $\tau_{k,n}$ correction are performed.

A 1D projection of the signal shows no significant improvement in chemical shift correction comparing panel (c) and panel (o):

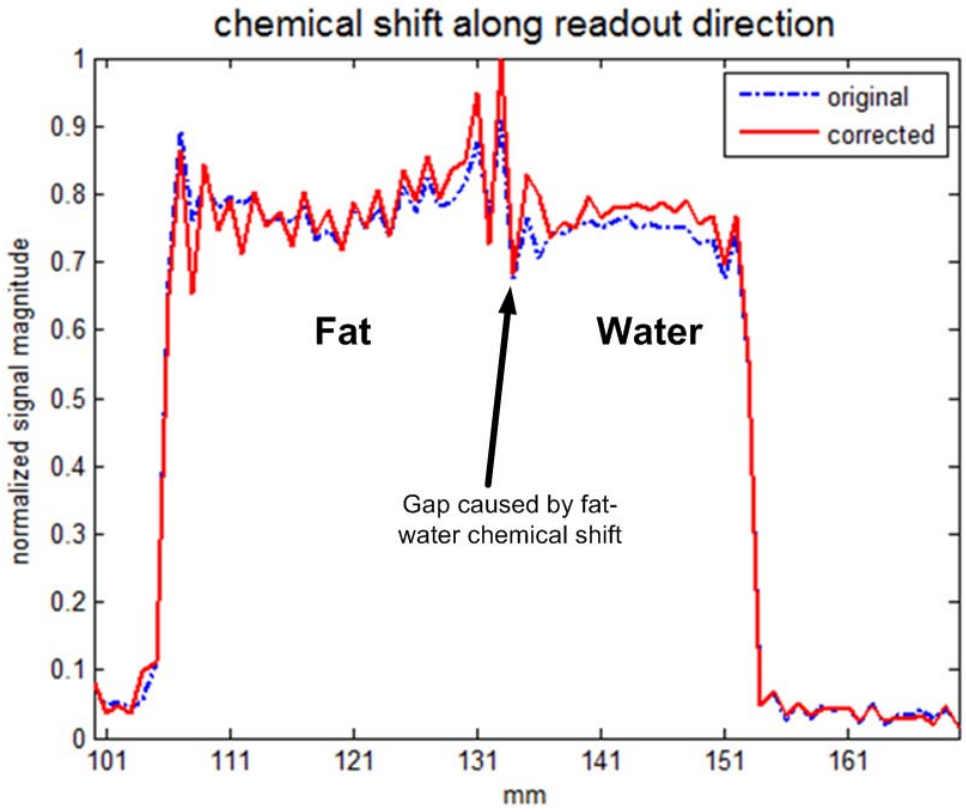

Figure 2.28. 1D projection profile of normalized signal strength of the mineral oil phantom along the center cut across the interface of the fat and water of the object.

Similarly, the separation result of peanut oil is shown in Figure 2.29:

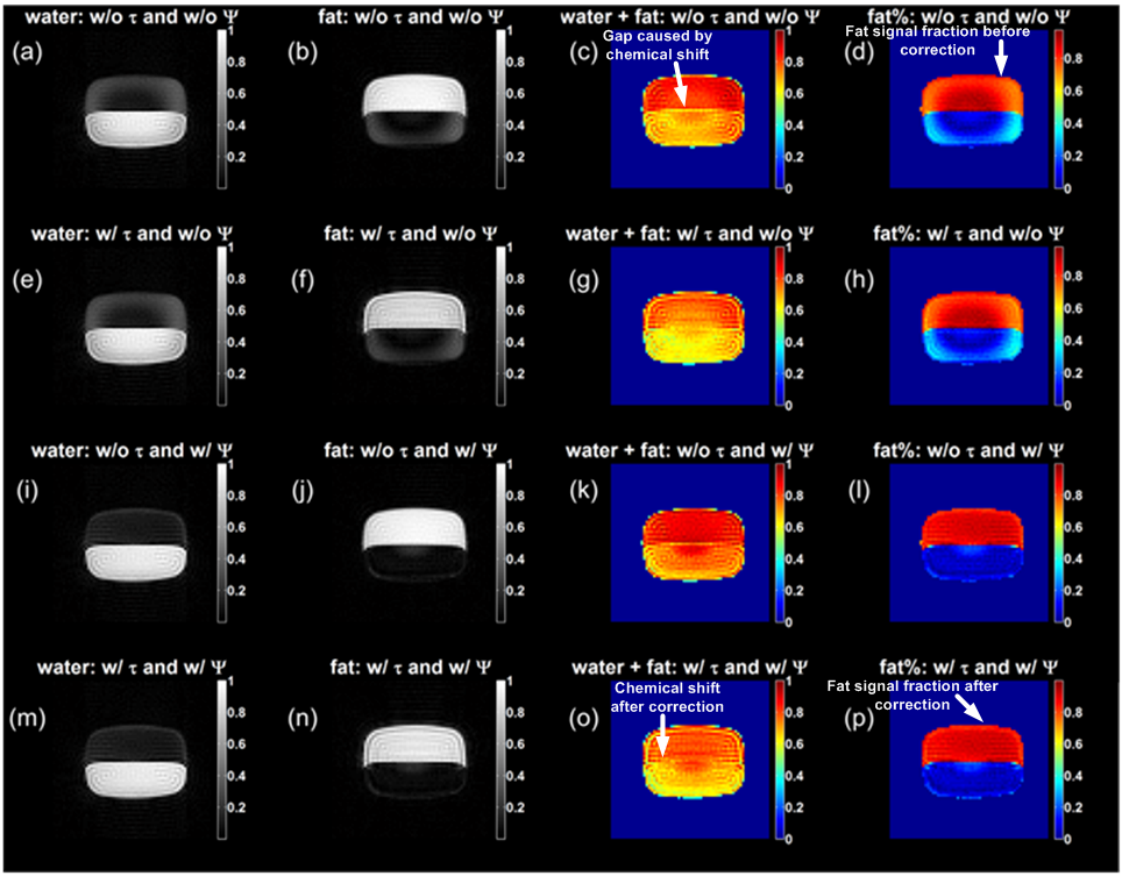

Figure 2.29. Peanut oil fat-water separation results from a radial acquisition: Panel (a) through (d) is water signal, fat signal, summation of fat and water signal, and fat signal percentage when there is neither $\tau_{k,n}$ map correction nor field inhomogeneity correction. Panel (e) through (h) is water signal, fat signal, summation of fat and water signal, and fat signal percentage when there is $\tau_{k,n}$ map correction but no field inhomogeneity correction. Panel (i) through (l) is water signal, fat signal, summation of fat and water signal, and fat signal percentage when there is no $\tau_{k,n}$ map correction but field inhomogeneity correction. Panel (e) through (h) is water signal, fat signal, summation of fat and water signal, and fat signal percentage with both $\tau_{k,n}$ map correction but and field inhomogeneity correction.

In Figure 2.29, more significant improvement occurs with the peanut oil than mineral oil. This particularly is noticeable from panel (d) through panel (p) as last column of the diagram. This also suggests that the peanut oil phantom experienced a more serious field inhomogeneity compared to the mineral oil phantom. The quantified fat signal percentage with each correction is listed in Table 2.4:

Table 2.4. Fat signal percentage with different corrections for the Cartesian peanut oil phantom.

corrections	w/o $\tau_{k,n}$; w/o ψ	w/ $\tau_{k,n}$; w/o ψ	w/o $\tau_{k,n}$; w/ ψ	w/ $\tau_{k,n}$; w/ ψ
Fat Signal Percentage	82.44%	82.55%	88.18%	88.29%

Table 2.4 shows clear signal strength increase as more corrections are included. Like results from Cartesian separation, the $\tau_{k,n}$ correction does not significantly improve fat signal percentage compared to field inhomogeneity correction. However, when both $\tau_{k,n}$ correction and field inhomogeneity correction are performed, the fat signal percentage increases from 82.44% to 88.29%. This is displayed from panel (d) through panel (p) in Figure 2.29

The chemical shift in panel (c) is corrected in panel (o) in Figure 2.29, which is more distinguished in a 1D projection shown in Figure 2.30:

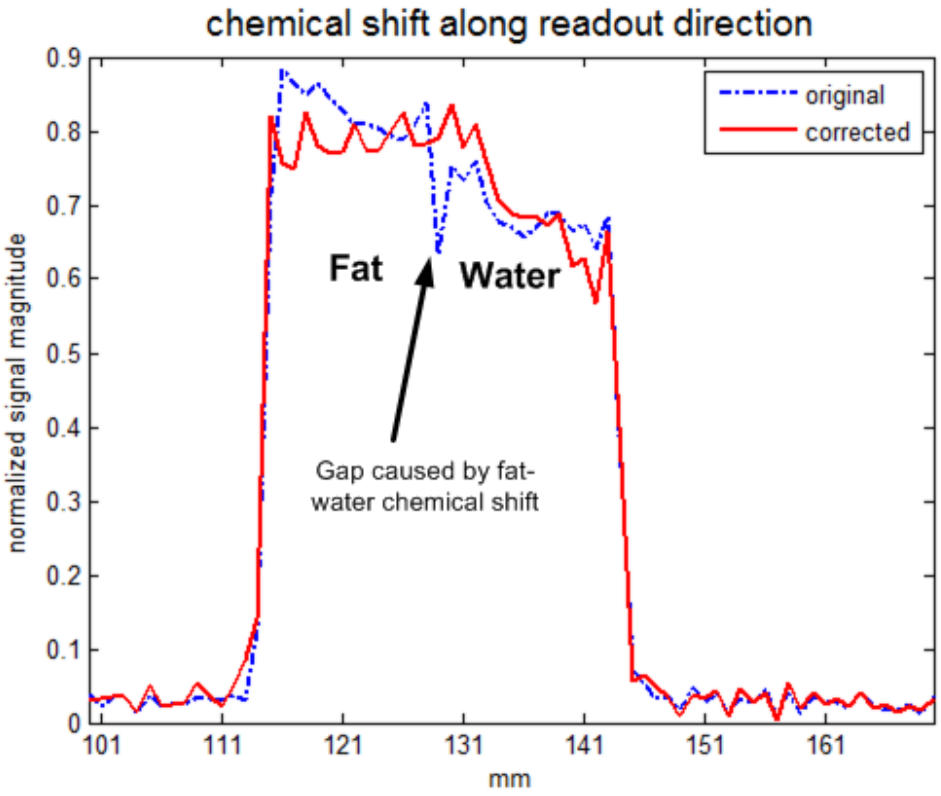

Figure 2.30. 1D projection profile of normalized signal strength of the peanut oil phantom along the center cut across the interface of the fat and water of the object.

The peanut oil phantom shows more improvement in chemical shift correction than mineral oil phantom. There is almost no gap after field inhomogeneity correction and $\tau_{n,k}$ map correction for the red curve in Figure 2.30.

2.5.4 Reversed Readout Gradient Correction of Field Inhomogeneity

In the previous sections, reconstruction results were shown for the fat-water phantoms acquired with radial trajectory. Prior knowledge of field map is calculated based on a separate Cartesian acquisition. However, the radial k-space data should itself contain information about the field inhomogeneity.

It was proposed by Chang in 1992 [12] that field inhomogeneity artifacts can be corrected along frequency encode direction if the readout gradient is reversed. When field inhomogeneity $\Delta B_0(x, y, z)$ is present at some location (x, y, z) in image space, the intra-slice image distortion that occurs along frequency encode direction in image space is shown in Equation 2.31 [12]:

$$x_1 = x + \frac{\Delta B_0(x)}{G_x} \tag{2.31}$$

where x is the true location of a signal in spatial domain, and x_1 is the distorted location due to inhomogeneity. When a reversed readout gradient is applied along the same frequency encode line, the new position becomes [12]:

$$x_2 = x + \frac{\alpha \Delta B_0(x)}{G_x}, \tag{2.32}$$

where α is the ratio of amplitude between the reversed readout gradient and the original.

On the other hand, the signal intensity at position x_1 and x_2 can be calculated as [12]:

$$i_1(x_1) = i(x)\frac{dx_1}{dx} \tag{2.33}$$

$$i_2(x_2) = i(x)\frac{dx_2}{dx} \tag{2.34}$$

where, $i_1(x_1)$ and $i_2(x_2)$ are image intensities at distorted location x_1 and x_2, and $i(x)$ is the

image intensity at undistorted location x. The distortion in image space caused by field inhomogeneity is illustrated in Figure 2.31 [12]:

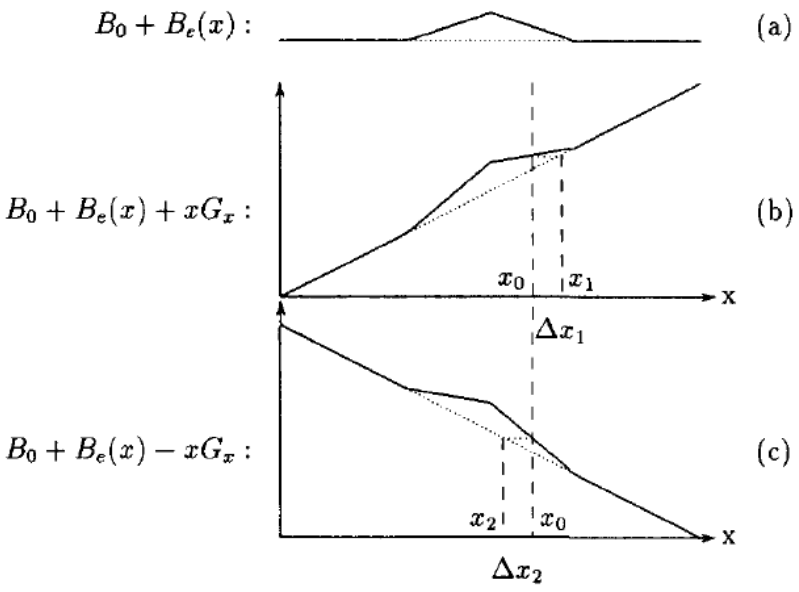

Figure 2.31. Image distortion caused by field inhomogeneity with G_x as readout gradient: (a) Static field B_0 superimposed with a disturbance $B_e(x)$; (b) Field inhomogeneity causes image distortion Δx defined as the displacement from its original location x_0 to x_1; (c) If the readout gradient is reversed, the distortion, as indicated as Δx, for x_0 will occur at x_2.

In Figure 2.31, when G_x is reversed to $-G_x$, the displacement of the true signal changes the location from x_1 to x_2. This suggests that along the frequency encode direction the true signal location should be somewhere between the signals with positive and reversed readout gradient.

Equation 2.25 through Equation 2.27 establish a relationship between the true image signal and the displaced signals caused by field inhomogeneity. This suggests that the true signal, or the undistorted image, can be estimated based on the information collected using readout

gradients reversed with respect to each other. Especially, when $\alpha = -1$, the true location of the undistorted signal, x, can be estimated as [12]:

$$x = \frac{x_1 + x_2}{2}, \tag{2.35}$$

and the true signal intensity $i(x)$ at location x can be estimated as [12]:

$$i(x) = \frac{2i_1(x_1)i_2(x_2)}{i_1(x_1) + i_2(x_2)}, \tag{2.36}$$

Equation 2.35 concludes that as long as x_1 and x_2 are known, the true location x can be estimated. In addition, it should be pointed out that every x_1 is paired with a particular x_2, although there is no straightforward information regarding how they are paired with each other. However, conclusion in Equation 2.36 can be solved from Equation 2.33 and Equation 2.34 by applying the chain rule [12]:

$$\frac{dx_2}{dx_1} = \frac{i_1(x_1)}{i_2(x_2)}, \tag{2.37}$$

Equation 2.37 is an ordinary differential equation (ODE) which can be solved with boundary conditions.

The Runge-Kutta-Fehlberg 5th order (RKF45) method [19] with adaptive step size was chosen as the numerical integration technique. The numerical method solves the position pairing from the original k-space data and from the average of its neighbours. For each projection pair, the original and the reversed, the integration method is applied to estimate the true location and intensity for each spatial domain projection sample. Figure 2.32 shows the

estimate of unbiased signal using RKF45 method:

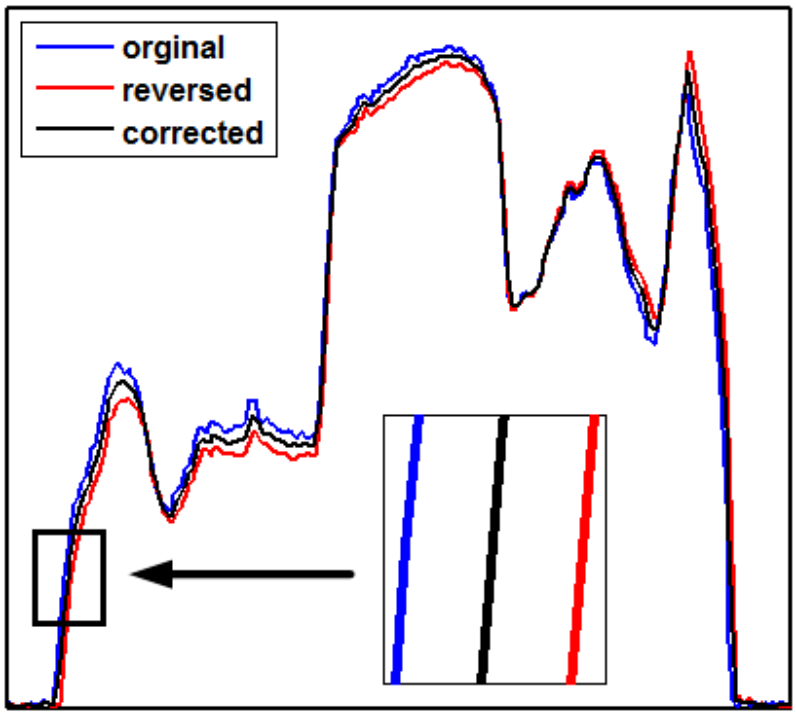

Figure 2.32. Estimate of unbiased signal (black curve, corrected) based on original signal (blue curve, original) and the reversed (red curve, reversed) using RKF45 method. Zoom-in window shows that the corrected signal is situated between the original and the reversed.

In our experiment, as illustrated in Figure 2.12, the radial readout lines are acquired in alternating directions. Since 201 readout lines are sampled, it is sufficiently precise to simulate the revered gradient approximation of a single readout line by averaging its closest neighboring pair, as illustrated in Figure 2.13. The two 1D data vectors, original k-space and its reversed readout approximation, were then both 1D Fourier transformed into the spatial domain (sinogram space).

In Figure 2.32, the “original” blue curve indicates one single projection in the original sinogram degraded by field inhomogeneity; the “reversed” red curve represents the same projection experiencing a reversed readout gradient; the “corrected” black curve is the estimated

trajectory of the unbiased projection with field inhomogeneity removed. A zoom-in window clearly shows the displacement, for blue and red curves from the black curve. The reversed readout gradient causes the blue curve and the red curve to locate on different sides of the black curve. It is also noticeable that the corrected curve lies almost exactly in the middle of original blue curve and reversed red curve, which is supported by Equation 2.35 and Equation 2.36.

Since the frequency encoding direction in radial MRI is the same as that for one single spatial projection according to the Fourier Projection-Slice Theorem, the field inhomogeneity correction of this approach is essentially operating in sinogram space. Figure 2.33 displays the improvement of a sinogram after RKF45 based correction is applied:

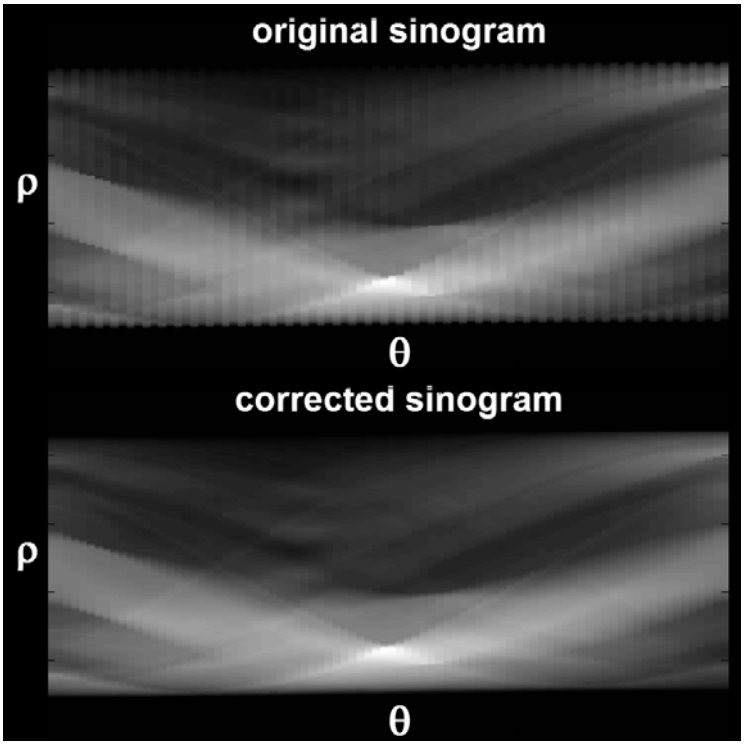

Figure 2.33. Comparison between sinogram before (top) and after (bottom) RKF45 correction is performed.

It is easily observed in Figure 2.33 that the corrected sinogram is smoother than the original because the zigzag pattern in the original sinogram (top) is significantly reduced in the corrected one (bottom).

After applying the correction to each projection and obtaining a corrected sinogram, the final image is reconstructed using NUFFT [18]. The numerical integration needs boundary conditions, which is implemented by thresholding to exclude the background region in each projection. Estimation of the final corrected projection samples was achieved using spline interpolation [20]. The method proposed in [12] did not account for complex numbers, so phase was estimated by averaging the real and the imaginary parts for the original data and its reversed readout approximation. The reconstruction results of a PIQT phantom is shown in Figure 2.34:

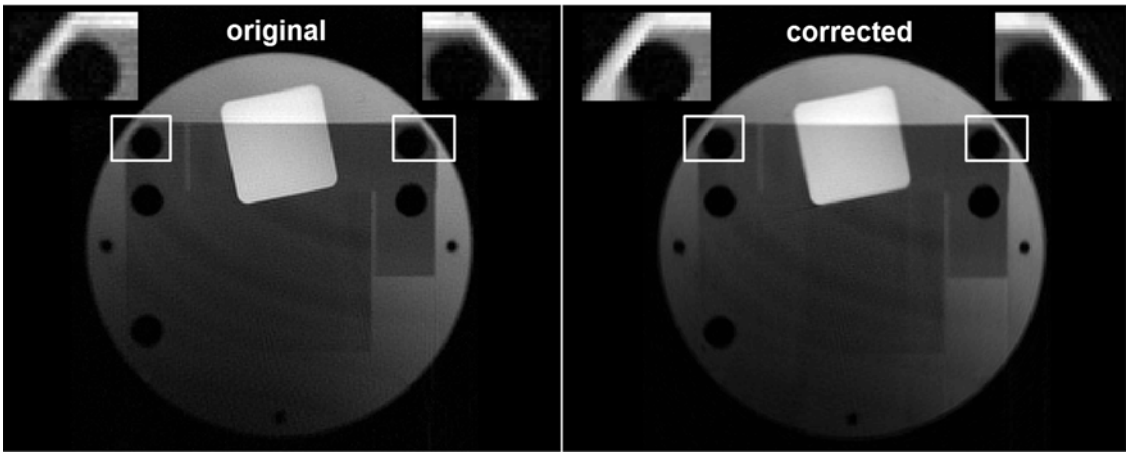

Figure 2.34. Comparison between original and corrected reconstruction for PIQT phantom.

Improvement is evident around the holes highlighted with white rectangles. Sharper features can be observed in the corrected image compared to the original image. This shows RKF 5th order integration with spline interpolation can improve the image reconstruction quality, which

was originally corrupted by the field inhomogeneity

2.6 Discussion

Fat-water separation has many pitfalls that require attention. Artifacts arise from many sources such as k-space sampling scheme, field inhomogeneity or chemical shift. In general, MRI image reconstruction consists of three major phases: preprocessing, reconstruction and post processing. A typical example of preprocessing in this work is the correction of artifact caused by alternating readout direction in this work. The raw radial k-space data are acquired with alternating readout direction, which causes k-space frequency encode lines to be misaligned with the center of the k-space. It should be mentioned alternating scan scheme was employed because there will be significant smearing of signal intensity across the FOV in the lipid image acquired with the radial technique if the standard scan direction is used [21]. Although reconstruction without shift correction yields acceptable image quality, results presented here show that improvements can still be made when phase correction is performed in the spatial domain. It should also be noticed that the feasibility of using Fourier shift theorem in this case is because same phase multiplication is imposed on all sampling positions along a projection in image space. Whereas in readout reversed gradient correction for radial MRI data, the displacement varies as location in image space changes. For image reconstruction, data sampled with radial trajectory are in general more difficult to process than those sampled with Cartesian trajectory, since more procedures, such as regridding, density correction and interpolation, are involved. Using the IDEAL method [15] to separate fat and water for *in vitro* phantoms is rather straightforward, but conducting same work for radial data is not as easy as for Cartesian data. One of the most challenging parts for radial data separation is how to accurately estimate the field inhomogeneity directly from raw data. In specific, the radial data are acquired based on line integral, or the summation of density along

a line, of the object. This makes it difficult to correct the field inhomogeneity corruption of the raw data. The reversed gradient method provides a way of correcting field inhomogeneity for radial data, but the pairing procedure is extremely sensitive to noise. Data need to be carefully processed. Extra steps, such as low-pass filtering before numerical integration and spline interpolation after numerical integration, are used to increase the robustness of the algorithm, although some resolution in spatial domain could be sacrificed. In addition, although the reversed gradient method has shown encouraging results for radial MRI raw data correction, using it to retrieve precise field map is still under investigation. Although some experiments have been conducted in this work, reliable field map estimation still relies on the IDEAL method.

In conclusion, the IDEAL method provides a reliable way to estimate field map for data sampled with Cartesian trajectory. Radial fat-water data correction needs accurate field map information to produce acceptable reconstruction results. Many detailed issues, such as direct estimation of field map for radial MRI data, are still open and are worthy of further work. On the other hand, non-Cartesian fat-water separation is a broad topic with which there is many directions to extend. It can be combined with other topics, some of which will be introduced in next chapter,

CHAPTER 3

FUTURE WORK

3.1 Future Work

Although Cartesian fat-water separation is an essential part of this work, radial MRI is the focus, especially with respect to future applications. Possible future work that will be benefit for clinical applications includes: 1 auto-calibrated parallel imaging; 2, sliding window helical spiral using golden angle radial acquisition with a continuous moving table.

In 2010 [22], Lin proposed an offline method, GRAPPA operator for wider radial bands (GROWL), for the reconstruction of undersampled radial MRI data. This GRAPPA [23] based method expands undersampled radial data to cover entire k-space using only the fully sampled central portion of the k-space (Nyquist circle) to estimate the GROWL operator. The expansion using the GROWL operator occurs to each radial line making them wider radial bands. Although the edges of k-space violate the Nyquist sampling criterion, the fully sampled signal inside the smaller Nyquist circle (Figure 3.1a) is sufficiently informative to calibrate the GROWL operator. The data after self-calibration will become fully sampled across the entire k-space. The basic principle of GROWL is depicted in Figure 3.1 [22]:

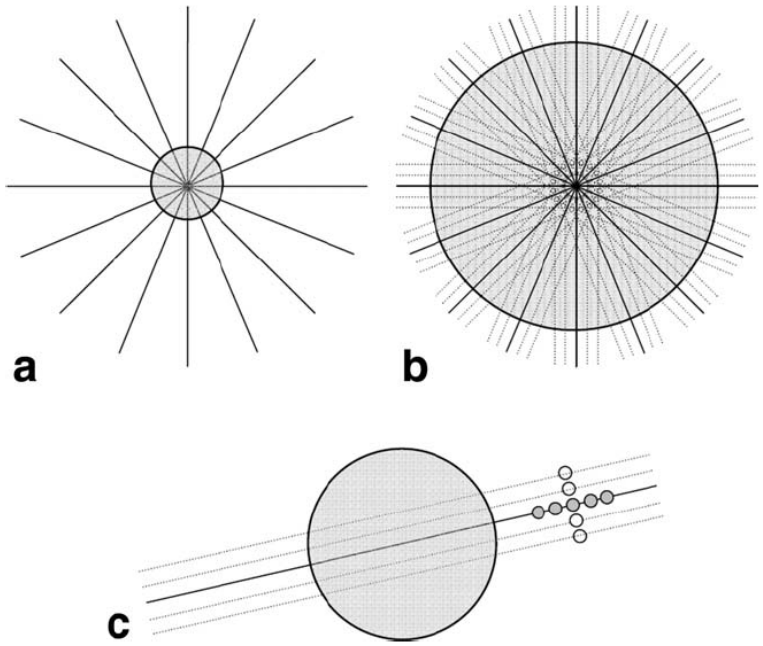

Figure 3.1. The basic idea of GROWL. a: undersampled radial k-space data with its central portion (Nyquist circle, highlighted in gray) inside which the Nyquist criterion is satisfied. b: each single projection is expanded by the GRAPPA relative shift operators to form a wider band, and the Nyquist circle is thus enlarged. c: for each single projection, calibration is first performed based on the information inside the Nyquist circle(the gray region), then GRAPPA relative shift operators mapping source (gray) points to target (white) points [22].

The optimal weights that solves for expanding source signal to targeting positions are determined by Tikhonov regularization in Equation 3.1 [24] [25]:

$$w_{opt} = \arg\min\left\{\left\|t_{ACS} - S_{ACS}w\right\|^2 + \lambda^2\left\|w\right\|^2\right\}, \qquad 3.1$$

where, w_{opt} is the optimal weights, $\left\|\cdot\right\|^2$ is the L_2 norm, the subscript ACS indicates that both target and source data points are collected in the ACS region, t_{ACS} is the targeting signal (white circles in Figure 3.1c), S_{ACS} is the source signal, w is the weight vector for the GRAPPA relative shift operator, and λ is the Tikhonov factor [22]. The solution to Equation 3.1 is described in Equation 3.2 [22]:

$$w_{opt} = \sum_{j=1}^{n} \frac{s_j}{s_j^2 + \lambda^2} u_j^H t v_j, \qquad 3.2$$

where u_j, v_j and s_j are the left singular vectors, right singular vectors, and singular values of S (source signal), respectively, generated by singular value decomposition, with singular vectors and singular values indexed by j [22].

It is also mentioned in [22] that the acceleration factor achievable with the GROWL reconstruction depends on the number of coil elements and noise levels in the data. Results in [22] show that 256×256 images with acceptable qualities can be reconstructed with 32 radial views, using a commercial eight-channel head coil and a low SNR condition. It is also pointed out in [22] that combination of different image processing techniques, such as GROWL and radial GRAPPA, or GROWL and PARS [26] (parallel imaging with augmented radius in k-space), is possible to achieve larger acceleration factors.

Another possible potential direction, as mentioned previously, focuses on sliding window helical spiral using gold ratio spaced acquisition. Although there have been many advanced reconstruction techniques created, some fundamental problems, such as sampling strategies, are still worth investigating.

In radial MRI, the dominant sampling structure is to sample the k-space with equally spaced readout lines, which can be traced back to Lauterbur's seminal paper in 1973 [27]. However, today many novel appliances for radial MRI have been developed in dynamic applications that require a high temporal resolution while tolerating an increased artifact level in return. As discussed in previous section, azimuthally undersampled radial data may therefore considerably increase the image acquisition rate without sacrifice significant information [28]. In addition, MRI data reconstruction acquired with a moving table along axial direction is

raising interests due to its potential for fast and subject-friendly scans. Sliding window reconstruction techniques already described in the literature can increase the image update rate or can balance spatial and temporal resolutions.

In 2007, a golden ratio based radial MRI sampling strategy was described in [28]. Instead of using evenly spaced readout lines, the k-space is sampled with readout lines rotating with fixed angular increment of $111.25°$, which is the ratio of $180°$ to golden ratio (1.618). The comparison between golden ratio sampling and traditional uniform sampling is shown in Figure 3.2 [28]:

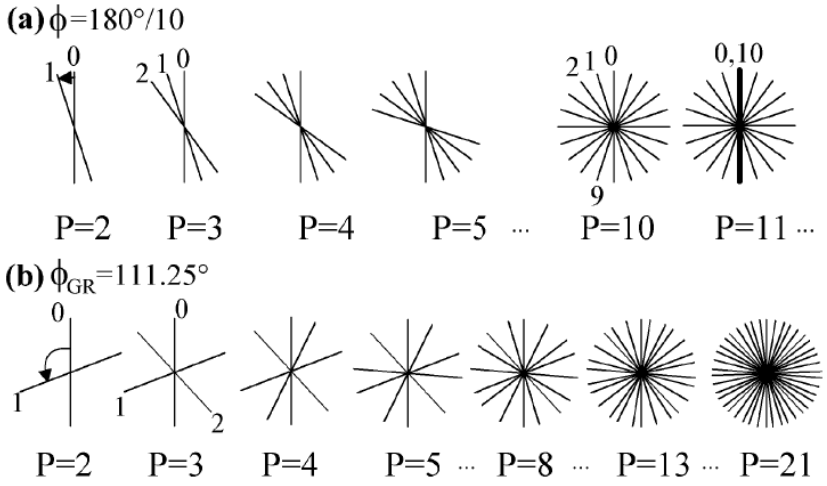

Figure 3.2. (a) Uniformly sampled radial data. P is the number of projections. k-space is either unevenly or excessively sampled unless P is equal to 10. (b) Golden ratio sampled radial data. P is the number of projections. Projections are evenly distributed regardless the value of P [28].

With this sampling scheme, the readout lines are almost evenly spaced across k-space for any arbitrary number of consecutive projection angles, especially when the number of the projections is equal to Fibonacci numbers.

For the uniform sampling strategy, the sampling trajectory either does not cover the entire k-space or oversamples the same line multiple times when number of the projections is too small or too large. This never occurs with the golden ratio sampling technique since the projections tend to evenly distribute across k-space, and they never overlap with each other.

It is also shown in [28] that in terms of SNR and residual error of the magnetization transfer function, the Golden Ratio based method and uniform sampling strategy have very similar performance.

The sampling scheme for radial MRI based on golden ratio projection angle spacing makes it possible to acquire and reconstruct data for an arbitrary length of time. In an arbitrarily long sampling window, projections are nearly evenly distributed across k-space. It is also possible that the k-space data may be undersampled. These approaches create the opportunity for undersampled radial MRI fat-water data acquired with a continuously moving table. This helical-spiral-like trajectory will eventually leads to faster and more efficient MR imaging technique.

One of its advantages is that its reconstruction will keep the majority of the image information even if some of the radial lines are skipped. This means decent reconstructions are possible for undersampled radial MRI data. On the other hand, instead of typical backfolding artifacts in Cartesian data, radial MRI reconstruction often just generates artifacts as streaks [6]. These merits of radial MRI make it specifically useful in dynamic applications where the total sampling duration is critical.

Nyquist sampling theorem requires the sampling frequency is no less than two times the maximum band width of the sampled signal. In radial MRI, this is satisfied if the distance or the azimuthal gap between two consecutive samples in azimuthal direction does not exceed

the sample distance in readout (or radial) direction [28]. However, fully sampled radial MRI data need density correction for its reconstruction due to the oversampled central portion of the k-space. Filters such as Ram-Lak are often used to weight down the central part of the radial k-space. Thus, even though radial k-space data are undersampled, the central portion of the k-space is still possible meet the Nyquist criterion. On the other hand the combination of a moving bed with a SENSE [29] (multi-channel) coil at isocenter through which the table moves. A radial acquisition would allow for auto-calibrated multi channel reconstruction in such a case.

In conclusion, this work started with Cartesian fat-water separation, and investigated fully sampled radial MRI data acquired with single channel. It studied various topics regarding data correction such as field inhomogeneity correction and non-perfect alternating scan correction for radial MRI. Future work is to successfully process chemical shift imaging for data acquired with multi-channel, with undersampled radial trajectory, and with a continuously moving table.

REFERENCES

[1] J. Keeler, *Understanding NMR Spectroscopy*. Wiley, 2005.

[2] David R. Lide, *CRC Handbook of Chemistry and Physics*, 90th ed. CRC, 2009.

[3] J. P. Hornak, *The Basics of MRI*. Interactive Learning Software, 2008.

[4] C. Westbrook, *MRI at a Glance*. Blackwell Science Ltd., 2002, pp. 20, 21.

[5] M. R. P. Donald W. McRobbie, Elizabeth A. Moore, Martin J. Graves, *MRI from Picture to Proton*. Cambridge University Press, 2003.

[6] D. G. Nishimura, *Principles of Magnetic Resonance Imaging*. Stanford University, 2010.

[7] K. T. Block, M. Uecker, and J. Frahm, “Undersampled radial MRI with multiple coils. Iterative image reconstruction using a total variation constraint.,” *Magnetic resonance in medicine : official journal of the Society of Magnetic Resonance in Medicine / Society of Magnetic Resonance in Medicine*, vol. 57, no. 6, pp. 1086-98, Jun. 2007.

[8] J. Hsieh, *Computed Tomography: Principles, Design, Artifacts and Recent Advances*, 2nd ed. SPIE Publications, 2009.

[9] J. Pauly, “Dixon Reconstruction,” *October*, no. 2, pp. 1-6, 2007.

[10] B. D. Coombs, J. Szumowski, and W. Coshow, “Two-point Dixon technique for water-fat signal decomposition with B0 inhomogeneity correction.,” *Magnetic resonance in medicine : official journal of the Society of Magnetic Resonance in Medicine / Society of Magnetic Resonance in Medicine*, vol. 38, no. 6, pp. 884-9, Dec. 1997.

[11] J. Ma, “Dixon techniques for water and fat imaging.,” *Journal of magnetic resonance imaging : JMRI*, vol. 28, no. 3, pp. 543-58, Sep. 2008.

[12] H. Chang and J. M. Fitzpatrick, “A technique for accurate magnetic resonance imaging in the presence of field inhomogeneities.,” *IEEE transactions on medical imaging*, vol. 11, no. 3, pp. 319-29, Jan. 1992.

[13] A. N. Moghaddam and H. Soltanian-zadeh, “Mapping of Magnetic field Inhomogeneity and Removal of its Artifact from MR Images,” *Image (Rochester, N.Y.)*, vol. 5032, pp. 780-787, 2003.

[14] Z. Zhang, “FIELD INHOMOGENEITY COMPENSATION IN HIGH FIELD MAGNETIC RESONANCE IMAGING (MRI),” University of Pittsburgh, 2006.

[15] S. B. Reeder et al., “Multicoil Dixon chemical species separation with an iterative least-squares estimation method.,” *Magnetic resonance in medicine : official journal of the Society of Magnetic Resonance in Medicine / Society of Magnetic Resonance in Medicine*, vol. 51, no. 1, pp. 35-45, Jan. 2004.

[16] E. K. Brodsky, J. H. Holmes, H. Yu, and S. B. Reeder, “Generalized k-space decomposition with chemical shift correction for non-Cartesian water-fat imaging.,” *Magnetic resonance in medicine : official journal of the Society of Magnetic Resonance in Medicine / Society of Magnetic Resonance in Medicine*, vol. 59, no. 5, pp. 1151-64, May. 2008.

[17] D. C. Peters, J. A. Derbyshire, and E. R. McVeigh, “Centering the projection reconstruction trajectory: reducing gradient delay errors.,” *Magnetic resonance in medicine : official journal of the Society of Magnetic Resonance in Medicine / Society of Magnetic Resonance in Medicine*, vol. 50, no. 1, pp. 1-6, Jul. 2003.

[18] J. A. Fessler, S. Member, and B. P. Sutton, “Nonuniform Fast Fourier Transforms Using Min-Max Interpolation,” vol. 51, no. 2, pp. 560-574, 2003.

[19] G. W. Ernst Hairer, Syvert P. Nørsett, *Solving Ordinary Differential Equations I: Nonstiff Problems*, Second. Springer, 2008.

[20] Schoenberg, “Contributions to the problem of approximation of equidistant data by analytic functions,” *Quart. Appl. Math.*, vol. 4, pp. 45–99 and 112–141, 1946.

[21] Z. Li et al., “Rapid water and lipid imaging with T2 mapping using a radial IDEAL-GRASE technique.,” *Magnetic resonance in medicine : official journal of the Society of Magnetic Resonance in Medicine / Society of Magnetic Resonance in Medicine*, vol. 61, no. 6, pp. 1415-24, Jun. 2009.

[22] W. Lin, F. Huang, Y. Li, and A. Reykowski, “GRAPPA operator for wider radial bands (GROWL) with optimally regularized self-calibration.,” *Magnetic resonance in medicine : official journal of the Society of Magnetic Resonance in Medicine / Society of Magnetic Resonance in Medicine*, vol. 64, no. 3, pp. 757-66, Sep. 2010.

[23] M. A. Griswold, R. M. Heidemann, and P. M. Jakob, “Direct Parallel Imaging Reconstruction of Radially Sampled Data Using GRAPPA with Relative Shifts Synopsis : Introduction :,” *Solutions*, vol. 11, pp. 2349-2349, 2003.

[24] A.-I. N. Tikhonov, *Solutions of ill-posed problems*. 1977.

[25] F.-H. Lin, K. K. Kwong, J. W. Belliveau, and L. L. Wald, “Parallel imaging reconstruction using automatic regularization.,” *Magnetic resonance in medicine : official journal of the Society of Magnetic Resonance in Medicine / Society of Magnetic Resonance in Medicine*, vol. 51, no. 3, pp. 559-67, Mar. 2004.

[26] E. N. Yeh, C. a McKenzie, M. a Ohliger, and D. K. Sodickson, “Parallel magnetic resonance imaging with adaptive radius in k-space (PARS): constrained image reconstruction using k-space locality in radiofrequency coil encoded data.,” *Magnetic resonance in medicine : official journal of the Society of Magnetic Resonance in Medicine / Society of Magnetic Resonance in Medicine*, vol. 53, no. 6, pp. 1383-92, Jun. 2005.

[27] P. Lauterbur, “Image Formation by Induced Local Interactions: Examples Employing Nuclear Magnetic Resonance,” *Nature*, vol. 242, pp. 190 - 191, 1973.

[28] S. Winkelmann, T. Schaeffter, T. Koehler, H. Eggers, and O. Doessel, “An optimal radial profile order based on the Golden Ratio for time-resolved MRI.,” *IEEE transactions on medical imaging*, vol. 26, no. 1, pp. 68-76, Jan. 2007.

[29] K. P. Pruessmann, M. Weiger, M. B. Scheidegger, and P. Boesiger, “SENSE: sensitivity encoding for fast MRI.,” *Magnetic resonance in medicine : official journal of the Society of Magnetic Resonance in Medicine / Society of Magnetic Resonance in Medicine*, vol. 42, no. 5, pp. 952-62, Nov. 1999.